Inorganic Chemistry

ARTICLE

pubs.acs.org/IC

Redox Noninnocence of Nitrosoarene Ligands in Transition Metal Complexes

Neil C. Tomson,[†] Liezel A. Labios,[‡] Thomas Weyhermüller,[†] Joshua S. Figueroa,*[,‡] and Karl Wieghardt*[,†]

[†]Max-Planck-Institut für Bioanorganische Chemie, Stiftstrasse 34-36, 45470 Mülheim an der Ruhr, Germany

[‡]Department of Chemistry and Biochemistry, University of California-San Diego, 9500 Gilman Drive, Mail Code 0358, La Jolla, California 92093-0358, United States

Supporting Information

ABSTRACT: Studies on the coordination of nitrosoarene (ArNO) ligands to late-transition metals are used to provide the first definition of the geometric, spectroscopic, and computational parameters associated with a PhNO electron-transfer series. Experimentally, the Pd complexes $PdCl_2(PhNO)_2$, $PdL_2(PhNO)_2$, and $PdL_2(TolNO)$ (L = $CNAr^{Dipp2}$; Ar^{Dipp2} = 2,6-(2,6-$^iPr_2C_6H_3$)$_2$-C_6H_3) are characterized as containing $(PhNO)^0$, $(PhNO)^{\bullet 1-}$, and $(TolNO)^{2-}$ ligands, respectively, and the structural and spectroscopic changes associated with this electron transfer series provide the basis for an extensive computational study of these and related ArNO-containing late-transition metal complexes. Most notable from the results is the unambiguous characterization of the ground state electronic structure of $PdL_2(PhNO)_2$, found to be the first isolable, transition metal ion complex containing an η^1-*N*-bound π-nitrosoarene radical anion. In addition to the electron transfer series, the synthesis and characterization of the Fe complex $[Fe(TIM)(NCCH_3)(PhNO)][(PF_6)_2]$ (TIM = 2,3,9,10-tetramethyl-1,4,8,11-tetraazacyclotetradeca-1,3,8,10-tetraene) allows for comparison of the geometric and spectroscopic features associated with metal-to-ligand π-backbonding as opposed to $(PhNO)^{\bullet 1-}$ formation. Throughout these series of complexes, the N−O, M−N, and C−N bond distances as well as the N−O stretching frequencies and the planarity of the ArNO ligands provided distinct parameters for each ligand oxidation state. Together, these data provide a delineation of the factors needed for evaluating the oxidation state of nitrosoarene ligands bound to transition metals in varying coordination modes.

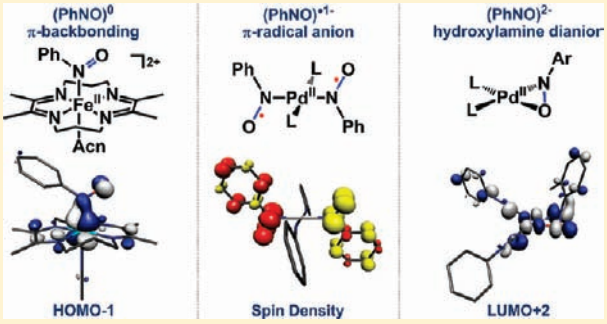

1. INTRODUCTION

The ability of some ligands to behave as redox-active partners with transition metals is predicated in part on the close energy of the metal-d and ligand-frontier orbitals. In many cases this energetic constraint requires conjugated, multidentate ligand-based π-systems, such as those found in 1,2-dithiolenes,[1] α-diimines,[2] 2,6-diimino-pyridines,[3] and others.[4] However, the relatively low-energy π^* orbitals of much simpler ligands, such as O_2 and NO, also allow for rich metal−ligand redox chemistry and have provided for fundamental advances in inorganic and biological chemistry.

C-organonitroso (RNO) compounds constitute a closely related class of redox-active ligands for transition metals.[5] This redox noninnocent behavior is readily predictable from the largely unperturbed nature of the out-of-plane π^*-orbital of free RNO compounds as compared to the π^* orbitals of free NO. It is therefore remarkable that the redox-activity of RNO as a ligand has received relatively little attention compared to that of O_2 and NO, especially considering both the biological importance of the closely related HNO ligand,[6−8] as well as the diverse and complex coordination chemistry of RNO ligands on transition metals in general.[9,10] This discrepancy may be partially due to the reported instability of transition-metal nitroxides (η^1-*N*-$[RNO]^{\bullet 1-}$-M) under common reaction conditions, which is evidenced in part by the surprisingly consistent lack of data on these compounds apart from that obtained by electron paramagnetic resonance (EPR) spectroscopy.[11]

Still, the documented variations in ligand binding modes and metric parameters for RNO-containing complexes seem to indicate that considerable ligand-based redox chemistry may have been overlooked in the literature. Recent interest in metal−ligand and ligand−ligand singlet diradical descriptions of complexes with redox-active ligands has highlighted the need for clear metric and spectroscopic handles for distinguishing between when the ground-state of a molecule is better described by two (or more) antiferromagnetically coupled radicals as opposed to the more common closed-shell orbital structure,[12] a distinction which has had major implications for the same aforementioned fields of chemistry.[13−15]

Received: March 23, 2011
Published: May 25, 2011

Scheme 1

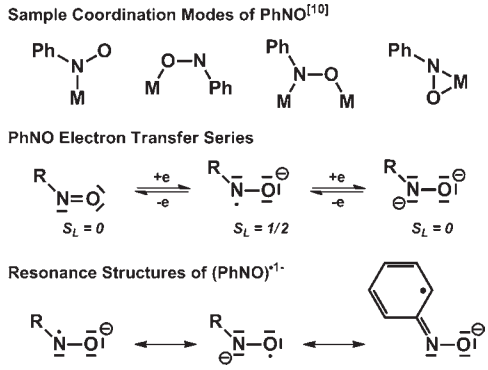

Previous experimental reports have characterized the π radical anion $(RNO)^{\bullet 1-}$ (R = alkyl, aryl) as both a transient product resulting from the one-electron reduction of free RNO species[16−22] and as a η^1-*N*-bound ligand for transition metal complexes, resulting from the use of RNO as a stabilizing "spin-trap" for reactive transition-metal-based radicals.[11] These latter studies find analogy with the use of RNO compounds as "spin-traps" for organic radicals, but, importantly, η^1-*N*-$(RNO)^{\bullet 1-}$ complexes of transition metals have never been isolated and have not been characterized apart from in situ EPR spectroscopic studies. To the best of our knowledge, only the bimetallic complexes $[\{Cp^*M(\mu\text{-}S^iPr)\}_2(\mu\text{-}1\kappa^1N{:}2\kappa^1O\text{-}PhNO)][X]$ (M = Ru, Rh, Ir; X = OTf, BPh_4) have been isolated, fully characterized, and ultimately described as $(PhNO)^{\bullet 1-}$-containing transition-metal species.[23]

Herein we report on our assignment of a range of isolable nitrosobenzene complexes as containing either (1) a neutral $(PhNO)^0$ ligand ($S = 0$, η^1-*N* coordinated to a transition metal ion), (2) a monoanionic π-radical $(PhNO)^{\bullet 1-}$ ($S = 1/2$, η^1-*N*), or (3) a diamagnetic dianion $(PhNO)^{2-}$ ($S = 0$; η^2-*N*,*O*), which corresponds to an *N*,*O*-doubly deprotonated hydroxylamine (Scheme 1). These three forms constitute a three-membered electron transfer series, and this report represents the first in which all three members of this series have been isolated and fully characterized within a homologous series of complexes, thus allowing for a clear delineation of the geometric and electronic structure changes involved in RNO reduction. In addition to this experimental work, we have also performed an extensive theoretical study to understand the electronic origin of the observed structural changes across both the three-membered electron transfer series mentioned above as well as a range of related transition metal compounds.

2. EXPERIMENTAL SECTION

2.1. General Procedures. All experiments and manipulations were carried out under dry and oxygen-free conditions, using either standard Schlenk techniques or an inert atmosphere (dinitrogen) glovebox. Protiated solvents were either dried by passage through a column of activated alumina and sparged with argon prior to use or distilled from a purple solution of Na^0/benzophenone under an inert atmosphere. The compounds $[(tim)Fe(NCMe)_2][(PF_6)_2]$,[24] $K_3[(NC)_5Co(PhNO)]$,[17] and **1**−**4**[25,26] were prepared according to the previously published procedures. All other reagents were obtained from commercial sources and used without purification.

2.2. Synthesis of Pd(η^2-*O*,*N*-TolNO)$(CNAr^{Dipp2})_2$ (5). To an Et_2O solution of $Pd(CNAr^{Dipp2})_2$ (0.100 g, 0.105 mmol, 5 mL) was added an Et_2O solution of 2-nitrosotoluene (0.013 g, 0.110 mmol, 5 mL, 1.05 equiv). Upon addition, the reaction mixture immediately changed from orange to red. The reaction mixture was stirred for 15 min, and then all volatile materials were removed under reduced pressure. Dissolution of the resulting red residue in pentane followed by filtration produced dark red crystals within 1 h at room temperature, which were collected and dried in vacuo. Yield: 0.074 g, 0.069 mmol, 66%. ^{1}H NMR (500.1 MHz, C_6D_6, 20 °C): δ = 7.32 (t, 4H, J = 8 Hz, *p*-Dipp), 7.18 (d, 8H, J = 8 Hz, *m*-Dipp), 7.05 (d, 1H, J = 5 Hz, *m*-Tol), 7.04 (d, 1H, J = 5 Hz, *o*-Tol), 6.93−6.87 (m, 8H, *m*-Tol, *p*-Tol, *m*-Ph, and *p*-Ph), 2.62 (septet, 8H, J = 8 Hz, $CH(CH_3)_2$), 2.40 (s, 3H, ON-Tol-CH_3), 1.20 (br, 24H, J = 8 Hz, $CH(CH_3)_2$), 1.09 (d, 24H, J = 8 Hz, $CH(CH_3)_2$) ppm. $^{13}C\{^1H\}$ NMR (125.7 MHz, C_6D_6, 20 °C): δ = 160.9 (ON-C_{ipso}), 159.2 (*C*N), 146.4, 139.4, 134.4, 130.8, 130.1, 129.8, 128.4, 128.2, 128.0, 127.5, 125.9, 123.6, 31.4 ($CH(CH_3)_2$), 24.7 ($CH(CH_3)_2$), 24.3 ($CH(CH_3)_2$), 18.6 (ON-Tol-CH_3) ppm. FTIR (KBr pellet): (ν_{CN}) 2141 and 2112 cm^{-1}, also 3059, 2962, 2925, 2868, 1579, 1460, 1414, 1384, 1363, 1105, 1057, 805, 755 cm^{-1}. Analysis calculated for $C_{69}H_{81}N_3OPd$: C, 77.10; H, 7.60; N, 3.91. Found: C, 77.32; H, 7.73; N, 3.74.

2.3. Synthesis of [(TIM)Fe(PhNO)(NCMe)][$(PF_6)_2$] (6). An excess of solid PhNO (0.100 g, 0.934 mmol, 5.1 equiv) was added to a suspension of $[(tim)Fe(NCMe)_2][(PF_6)_2]$ (0.125 g, 0.185 mmol) in tetrahydrofuran (THF, 15 mL) at room temperature. The slurry was stirred rapidly for 12 h, over which time the color slowly turned from magenta to dark purple. Addition of pentane resulted in precipitation of the product as a purple solid, leaving a green-blue solution colored by free PhNO. Filtration, followed by washing with pentane to remove any remaining traces of unligated PhNO provided the product in 92% yield (0.126 g, 0.170 mmol). Crystallization by diffusion of Et_2O into an acetone solution of the product at room temperature provided large block-like crystals suitable for analysis by X-ray diffraction. ^{1}H NMR (400.1 MHz, $(D_3C)_2CO$, 20 °C): δ = 7.52 (t, 1H, *p*-Ph), 7.41 (t, 2H, *m*-Ph), 6.95 (d, 2H, *o*-Ph), 3.84 (m, 8H, MeC=NCH_2CH_2), 2.79 (s, 12H, *Me*C=NCH_2CH_2), 2.09 (s, 3H, *Me*C≡N−Fe), 1.84 (m, 4H, MeC=NCH_2CH_2) ppm. ^{13}C NMR (100.6 MHz, $(D_3C)_2CO$, 20 °C): δ = 182.0, 168.1, 137.0, 130.9, 130.1, 118.6, 52.7, 30.1, 27.1, 19.1 ppm. FTIR (KBr pellet): ν_{NO} = 1384, 1375, and 1363 cm^{-1}, also 2949, 2324, 2297, 1629, 1586, 1477, 1437, 1327, 1285, 1262, 1212, 1180, 1160, 1092, 1023, 1002, 990, 914, 834, 771, 741, 708, 668, 559 cm^{-1}. Analysis calculated for $C_{22}H_{32}F_{12}FeN_6OP_2$: C, 35.60; H, 4.35; N, 11.32. Found: C, 35.43; H, 4.34; N, 10.78.

2.4. Physical Methods. *2.4.1. Mössbauer Spectroscopy.* Mössbauer data were recorded on an alternating constant-acceleration spectrometer. The sample temperature was maintained at 80 K using an Oxford Instruments Variox. Isomer shifts are quoted relative to iron metal at 300 K. Data simulation was carried out using the program "MFIT", written by Dr. Eckhard Bill (Max Planck Institute for Bioinorganic Chemistry).

2.4.2. Magnetometry. Variable temperature (4−300 K) magnetization data were recorded in a 1 T magnetic field on a SQUID magnetometer (MPMS Quantum Design). The experimental magnetic susceptibility data were corrected for underlying diamagnetism using Pascal's constants, and an additional diamagnetic correction was applied to account for a diamagnetic impurity (free ligand) in the sample.

2.4.3. X-ray Absorption Spectroscopy. X-ray absorption spectra (XAS) measurements were conducted at the Stanford Synchrotron Radiation Lightsource (SSRL) with the SPEAR storage ring containing between 80 and 100 mA at 3.0 GeV. Pd K-edge data were collected on the structural molecular biology XAS beamline 7-3 operating with a wiggler field of 2 T. A Si(220) double-crystal monochromator was used. Beamline 7-3 is equipped with a rhodium-coated vertical collimating mirror upstream of the monochromator, and a downstream

dx.doi.org/10.1021/ic2005979 |*Inorg. Chem.* 2011, 50, 5763–5776

Table 1. Crystallographic Data for Compounds 5 and 6

	5	6
formula	$C_{71}H_{83}N_3O_{1.50}Pd$	$C_{22}H_{32}F_{12}FeN_6OP_2$
FW (g-mol^{-1})	1108.80	742.33
T (K)	100(2)	100(2)
λ (Å)	0.71073	0.71073
space group	$P\bar{1}$	$P2_1/c$
a (Å)	12.734(2)	18.192(2)
b (Å)	21.459(3)	11.7757(15)
c (Å)	23.750(4)	14.380(2)
α (deg)	83.733(2)	90
β (deg)	87.768(2)	107.262(2)
γ (deg)	85.113(2)	90
V (Å^3)	6424.7(17)	2941.8(6)
Z	4	4
ρ_{calcd} (g/cm^3)	1.146	1.676
μ (mm^{-1})	0.332	0.728
final R indices[a,b]	R_1 = 0.0527	R_1 = 0.0432
	wR_2 = 0.1227	wR_2 = 0.1100
R indices (all data)[a,b]	R_1 = 0.0763	R_1 = 0.0571
	wR_2 = 0.1346	wR_2 = 0.1228
Res. peak/hole (e$^-$/Å^3)	0.926/−0.622	1.221/−0.902
CCDC ref #	782971	782972

[a] Observation criterion: $I > 2\sigma(I)$; $R_1 = \Sigma||F_o| - |F_c||/\Sigma|F_o|$. [b] $wR_2 = [\Sigma w(F_o^2 - F_c^2)^2/\Sigma w(F_o^2)^2]^{1/2}$, where $w = 1/\sigma^2(F_o^2) + (aP)^2 + bP$ and $P = (F_o^2 + 2F_c^2)/3$.

bent-cylindrical focusing mirror (also rhodium-coated). Harmonic rejection was accomplished by detuning the intensity of the incident radiation at the end of the scan by 50%. Incident and transmitted X-ray intensities were monitored using argon- or nitrogen-filled ionization chambers. X-ray absorption was measured in transmittance mode. During data collection, samples were maintained at a temperature of approximately 10 K using an Oxford Instruments liquid helium flow cryostat. Internal energy calibrations were performed by simultaneous measurement of the Pd reference foil placed between the second and third ionization chamber with the inflection point assigned at 24350 eV. Data represent 3−5 scan averages and were processed by fitting a second-order polynomial to the pre-edge region and subtracting this background from the entire spectrum. A three-region cubic spline was used to model the smooth background above the edge. The data were normalized by subtracting the spline and normalizing the postedge to 1.0. Because of the indeterminate nature of the pre-edge transitions, the position of the edge for each compound was taken to be the energy at a normalized absorption intensity of 0.5.

*2.4.4. X-ray Crystallography of (η^2-TolNO)Pd(CNAr^{Dipp2})$_2$ (**5**).* A single-crystal X-ray structure determination (Table 1) was carried out at low temperature on a Bruker Platform Diffractometer equipped with a Bruker APEX II detector. The structure was solved by direct methods with SIR 2004[27] and refined by full-matrix least-squares procedures utilizing SHELXL-97.[28] The crystallographic routine SQUEEZE[29] was employed to account for a severely disordered molecule of diethyl ether (Et_2O). The solvent-free refinement information is detailed within the CIF for (η^2-TolNO)Pd(CNAr^{Dipp2})$_2$.

*2.4.5. X-ray Crystallography of [(TIM)Fe(PhNO)(NCMe)][(PF_6)] (**6**).* A single crystal of **6** was coated with perfluoropolyether, picked up with a nylon loop and mounted in the nitrogen cold stream of the diffractometer. Graphite monochromated Mo−Kα radiation (α = 0.71073 Å) from a Mo-target rotating-anode X-ray source was used. Final cell constants were obtained from least-squares fits of several thousand strong reflections. Intensity data were corrected for absorption using intensities of redundant reflections with the program SADABS.[30] The structure was readily solved (Table 1) by the Patterson method and subsequent difference Fourier techniques. The Siemens ShelXTL[31] software package was used for solution and artwork of the structure; ShelXL97[32] was used for the refinement. All non-hydrogen atoms were anisotropically refined, and hydrogen atoms were placed at calculated positions and refined as riding atoms with isotropic displacement parameters.

2.5. Computational Methods. All density functional theory (DFT) calculations were performed with the ORCA program package.[33] Geometry optimizations were carried out at either the BP86[34,35] or the B3LYP[36−38] level of DFT, and single-point calculations on the optimized geometries were performed using the B3LYP functional. Unless otherwise stated, the crystallographically determined molecular coordinates referenced in this paper were used as starting geometries for all optimization calculations.

The all-electron Gaussian basis sets developed by the Ahlrichs group[39,40] were used in all calculations. The particular choices of standard (def2-TZVP and def2-SV(P)) and auxiliary (def2-TZV/J, def2-TZVP/J, and def2-SV/J) basis sets[41,42] for each calculation are given below, with the auxiliary basis sets[43−45] (used to expand the electron density in the resolution-of-identity (RI) approach) being chosen to match the orbital basis. The zeroth-order regular approximation (ZORA) method[46−48] was implemented for all calculations involving Ru and Pd. For these calculations, the standard basis sets def2-TZVP and def2-SV(P) were replaced with ZORA-TZVP and ZORA-SV(P),[49] respectively. The DFT integration grid used for the COSX approximation was increased by one step from the default value, and the final grid was turned off. All calculations have been performed using an empirical van der Waals correction to the DFT energy,[50−52] and the Conductor-like Screening Model (COSMO)[53] has been applied to the calculations involving charged species.

The SCF calculations were tightly converged (1×10^{-8} E_h in energy, 1×10^{-7} E_h in the density change, and 5×10^{-7} in the maximum element of the DIIS error vector). In all cases the geometries were considered converged after the energy change was less than 1×10^{-6} E_h, the gradient norm and maximum gradient element were smaller than 3×10^{-4} E_h-Bohr^{-1} and 1×10^{-4} E_h-Bohr^{-1}, respectively, and the root-mean square and maximum displacements of all atoms were smaller than 6×10^{-4} Bohr and 1×10^{-3} Bohr, respectively. The geometry optimizations for all complexes were carried out in redundant internal coordinates without imposing symmetry constraints, except in the case of the nonplanar form of PhNO, for which the unconstrained optimized geometry was used as a starting point, but the O−N−C−C dihedral angle was changed to 90°; the subsequent geometry optimization run was performed by constraining the dihedral angle as indicated.

For complex **6**, the Mössbauer spectral parameters (isomer shifts and quadrupole splittings) were calculated by performing a nonrelativistic single-point calculation on the optimized geometry, with the CP(PPP)[54] basis set for Fe. The Mössbauer isomer shifts were calculated from the computed electron density at the Fe center, as previously described.[55]

We have described the computational results for compound **4** using the broken symmetry (BS) approach of Ginsberg[56] and Noodleman et al.[57] Because several broken symmetry solutions to the spin-unrestricted Kohn−Sham equations may be obtained, the general notation BS(m,n)[58] has been adopted, where m(n) denotes the number of spin-up (spin-down) electrons at the two interacting fragments. Canonical, unrestricted-corresponding (UCO),[59] and quasi-restricted (QRO)[60] orbitals (iso-electron density surfaces = 95%) as well as spin density plots (iso-electron density surfaces = 99.5%) were generated with the program Molekel, v4.3.[61] The magnetic coupling J was calculated using the method developed by Yamaguchi and coworkers (eq 1).[62,63]

$$J = \frac{E_{HS} - E_{BS}}{\langle \hat{S}^2 \rangle_{HS} - \langle \hat{S}^2 \rangle_{BS}} \quad (1)$$

dx.doi.org/10.1021/ic2005979 |Inorg. Chem. 2011, 50, 5763–5776

Scheme 2

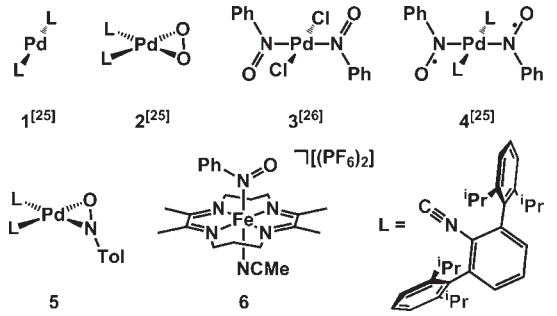

3. SYNTHETIC AND SPECTROSCOPIC RESULTS

3.1. $(ArNO)^{0/\bullet 1-/2-}$ Electron Transfer Series on Four-Coordinate Pd Complexes. Scheme 2 displays a series of five mononuclear palladium complexes. The diamagnetic complexes **1**, **2**, **3**, and **4** have been previously synthesized and structurally characterized by X-ray crystallography.[25,26] The diamagnetic two-coordinate complex **1** contains a central Pd(0) (d^{10}) with two neutral isocyanide ligands. Its reaction with O_2 yields **2**, containing a square-planar Pd(II) ion (d^8, $S_{Pd} = 0$) and a side-on coordinated peroxide dianion (the O−O distance of 1.415(4) Å is typical for a single bond).

Interestingly, **1** also reacts with PhNO, generating **4**, which contains two η^1-*N*-bound PhNO groups in *trans*-positions and two neutral isocyanide ligands.[25] Some structural and spectroscopic properties of **4** are remarkable: (*i*) the N−O bond at 1.291 Å is significantly longer than in Balch's complex, **3**, which contains two *neutral* PhNO ligands, having N−O bond distances of 1.209 Å,[26,64] (*ii*) the geometry around the central Pd in **4** is square planar (Σ(angles about Pd) = 360.0°), indicating the presence of a Pd(II) ion, but (*iii*) the Pd−N distances of 2.011(2) Å (avg.) are consistent with Pd−N single bonds and do not differ significantly from the Pd−N bond distances in **3** at 1.994(2) Å. These parameters are consistent with differing oxidation levels of the PhNO ligands in **3** and **4**, a claim that is further supported by the infrared spectral data, for which the ν(NO) stretching frequency for **3** can be assigned to a band located at 1496 cm^{-1}, while that for **4** arises at 1316 cm^{-1}.

On the basis of these data, two electronic structure possibilities were proposed for **4** in the original report.[25] The first description was that of a closed-shell complex featuring a divalent Pd(II) ion and two nondegenerate π^* orbitals, each of which contain contributions from both PhNO units (a_u and a_g in idealized-C_i symmetry). NO bond reduction in this case arises from the presence of an electron pair in the lower-energy, ligand-based a_u orbital.[25] A second proposal for the electronic structure was also mentioned that of a singlet diradical ground state, featuring a Pd(II) center with two antiferromagnetically coupled $(PhNO)^{\bullet 1-}$ monoanionic radicals. Importantly, however, the *spin-restricted* DFT calculations reported previously, which were consistent with the closed-shell description, were not suitable for distinguishing between these two possibilities.

To experimentally distinguish between the proposed electronic structures, we have recorded the temperature dependence (3−300 K) of the magnetic susceptibility of a solid sample of **4** (Figure 1) and found that the complex is *paramagnetic* at room temperature. It displays a temperature-dependent magnetic moment of ∼1.9 μ_B at 300 K which decreases gradually over a broad temperature range, reaching ∼0.3 μ_B at 4 K. These data are readily fitted using a diradical model with two N-coordinated $(PhNO)^{\bullet 1-}$ radicals ($S_{rad} = 1/2$) and a diamagnetic central Pd(II) ion (d^8, $S_{Pd} = 0$). This diradical possesses an $S = 0$ ground state and an $S = 1$ excited state, and the experimentally established coupling constant J is found to be −115(2) cm^{-1} ($H = -2J \cdot S_1 \cdot S_2$, $S_1 = S_2 = 1/2$, $g = 2.0$). Thus, while much effort has been put toward the study of nitrosoarenes as spin-traps for transition metal-based radicals, complex **4** is the first η^1-*N*-$(PhNO)^{\bullet 1-}$-containing complex to be isolated and structurally characterized.

Complexes **3** and **4** constitute the first two members of a possible three-membered electron transfer series comprising

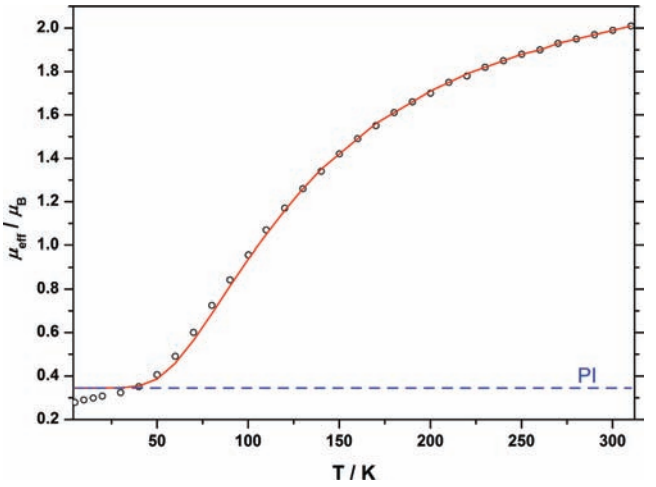

Figure 1. SQUID magnetometry data of **4** (open circles) along with simulated data (red line). Fixed simulation parameters: Spin 1 = Spin 2 = 0.5; $g_1 = g_2 = 2.000$; $\chi_{dia} = -800.0 \times 10^{-6}$ emu. Fit variables: $J_{12} = -115.1$ cm^{-1}; paramagnetic impurity ($S = 0.5$) = 4.0%; temperature-independent paramagnetism (TIP) = 4.8×10^{-6} emu.

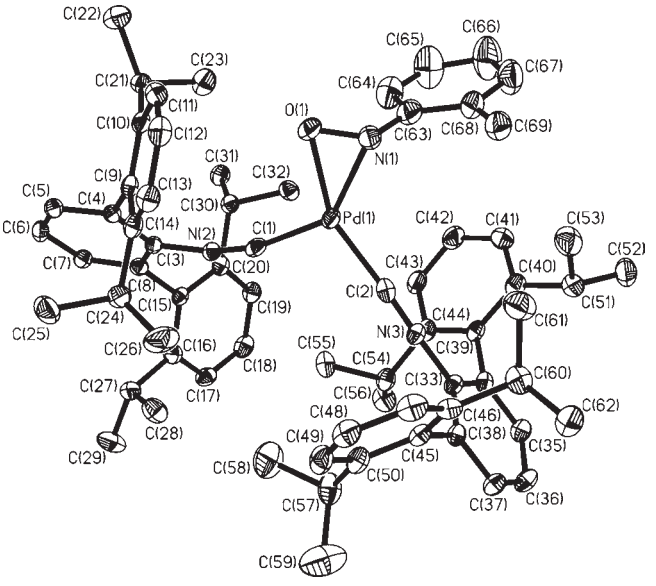

Figure 2. Crystal structure of **5**; thermal ellipsoids (50%) plot. Selected bond distances [Å] for one of the two crystallographically independent molecules: Pd−C1 2.010(4), Pd−C2 1.971(4), Pd−O1 2.021(3), Pd−N1 2.079(3), N1−O1 1.364(4).

dx.doi.org/10.1021/ic2005979 |*Inorg. Chem.* 2011, 50, 5763–5776

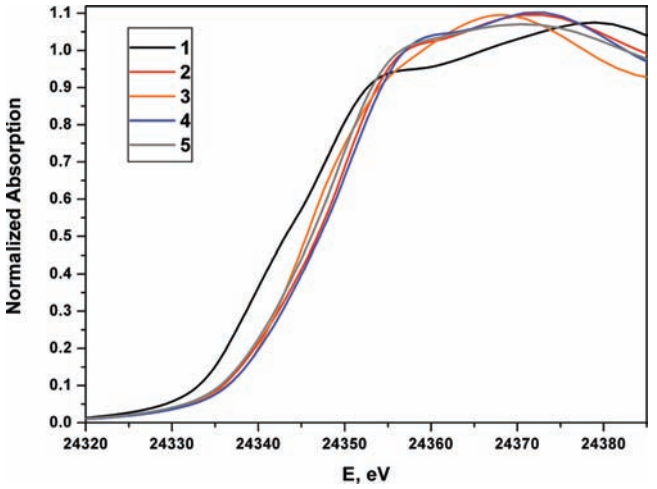

Figure 3. Comparison of the normalized Pd K-edge XAS spectra of **1** (black), **2** (red), **3** (orange), **4** (blue), and **5** (gray).

$(PhNO)^{0/\bullet 1-/2-}$. By treating **1** with TolNO we have been able to isolate a Pd complex in which a nitrosoarene is bound in the $(TolNO)^{2-}$ oxidation state, thus fulfilling the electron transfer series. The product, **5** (Scheme 2), contains a single η^2-*N*,*O*-TolNO ligand coordinated to a square-planar Pd center (Σ(angles about Pd) = 360.0°); the two isocyanide ligands now adopt a *cis* configuration, with a C−Pd−C angle of 104°. The first example of a metallaoxaaziridine was that of $[Mo^{VI}O(pic)(HMPA)(\eta^2\text{-}PhNO^{2-})]^0$ (S = 0) in which the N−O distance was reported to be 1.416(7) Å, clearly indicative of an N−O single bond.[65] More recent reports have suggested the presence of η^2-PhNO ligands on Ni,[66−68] Pd,[68] and Pt,[68−70] but crystallographic data are only available for the square-planar complex $Pt(\eta^2\text{-}PhNO)(PPh_3)_2$,[71] for which the N−O distance is again consistent with an N−O single bond (1.410 Å).[72] The N−O distance in **5** of 1.359(3) Å (Figure 2) is long compared to the η^1-*N*-$(PhNO)^{\bullet 1-}$ complexes described in this work. This parameter and the square-planar coordination environment about the metal center indicate that this species also contains a doubly-*N*, *O*-deprotonated derivative of *N*-arylhydroxylamine.[73] The slightly shorter N−O bond length in **5**, relative to $[Mo^{VI}O(pic)(HMPA)(\eta^2\text{-}PhNO^{2-})]^0$ and $Pt(\eta^2\text{-}PhNO)(PPh_3)_2$, results from the presence of the π-acidic isocyanide ligands (see Computational Results below).

To obtain more direct experimental data on the oxidation state of the Pd atoms in complexes **1**−**5** and indirect evidence for the extent of reduction of the coordinated PhNO units, Pd K-edge XAS were recorded (Figure 3, Table 2). As opposed to 1s→3d pre-edge features, which are often used for comparing oxidation states within a series of complexes, the position of the rising edge is not as sensitive to the coordination number about the metal center and therefore allows for a more direct comparison between the two-coordinate Pd complex **1** and the four-coordinate complexes **2**−**5**. The rising Pd K-edge energy of **1** is lowest whereas the corresponding energies of **2**−**5** are 2.4−4.0 eV higher in energy. As an increase of the rising edge energy by 1.2−2.0 eV is typical for an increase of oxidation state by one unit, we conclude that in complexes **2**−**5** the Pd center is a divalent ion whereas the central Pd atom in **1** has an oxidation state of zero.

Table 2. Pd K-Edge X-ray Absorption Spectra of Complexes 1−5

complexes	energy of the Pd rising edge, eV	$\lvert\Delta E\rvert$, eV[a]
1	24343.2	0
2	24346.9	3.7
3	24345.6	2.4
4	24347.2	4.0
5	24346.3	3.1

[a] Energy difference between the Pd rising edge energy of **1** (Pd^0) and the other complexes given (Pd^{II}).

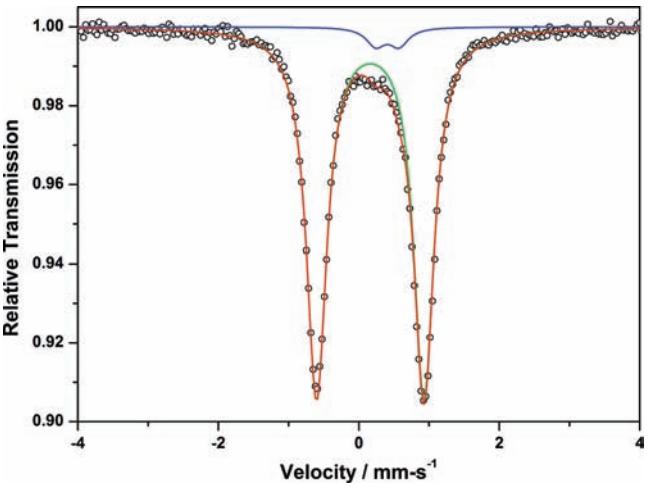

Figure 4. Zero-field Mössbauer spectrum of **6**, collected at 80 K; experimental data (open circles), majority component (**6**, green line, 95.6%), minority component (blue line, 4.4%), summation of simulated components (red line).

3.2. η^1-*N*-$(PhNO)^0$ with π-Backbonding. Investigation of the literature on nitrosobenzene complexes of transition metals reveals that many such complexes exhibit N−O and C−N bond lengths intermediate between the values we have assigned for $(PhNO)^0$ (**3**) and $(PhNO)^{\bullet 1-}$ (**4**), which suggests a π-back-bonding interaction between the metal center and the PhNO ligand. Unfortunately, the weak π-basicity of Pd^{II} prevents our observation of this effect in any Pd species related to our series of complexes **1**−**5**. Thus to observe this effect and to obtain direct experimental data on the structural and spectroscopic features of PhNO ligands involved in strong metal-to-ligand π-backbonding as opposed to ligand reduction, we pursued PhNO coordination to a metal center both with higher-energy d-orbitals than Pd and in a geometry that prevented η^2-*N*,*O*-PhNO coordination.

The reaction of the diamagnetic, low-spin ferrous complex $[Fe^{II}(TIM)(NCCH_3)_2][(PF_6)_2]$ with PhNO yielded the diamagnetic species $[Fe^{II}(TIM)(PhNO)(NCCH_3)][(PF_6)_2]$ (**6**). The zero-field Mössbauer spectra of the starting material[74] and **6** at 80 K are very similar (Figure 4, Table 3), consistent with the presence of a low-spin Fe(II) ion in both complexes. The structure of **6** has been determined by X-ray crystallography, and the dication is shown in Figure 5. Using previously reported values for the correlation between bond lengths within the α-diimine portion of TIM and the oxidation state of the ligand,[74] we assign the macrocycle a neutral oxidation state, which implies that the oxidation state of PhNO is also neutral.

dx.doi.org/10.1021/ic2005979 |*Inorg. Chem.* 2011, 50, 5763–5776

Table 3. Experimental and Calculated Zero-Field Mössbauer Parameters for Related Fe Complexes in an Octahedral N_6 Donor Environment

complexes	δ, mm-s^{-1}	ΔE_Q, mm-s^{-1}
$[Fe(TIM)(NCCH_3)_2][(PF_6)_2]$[74] (experimental, collected at 80 K)	0.36	1.49
$[Fe(TIM)(PhNO)(NCCH_3)][(PF_6)_2]$ (**6**, experimental, collected at 80 K)	0.16	1.53
$[Fe(TIM)(PhNO)(NCCH_3)]^{2+}$ (**6**, calculated)	0.12	1.11

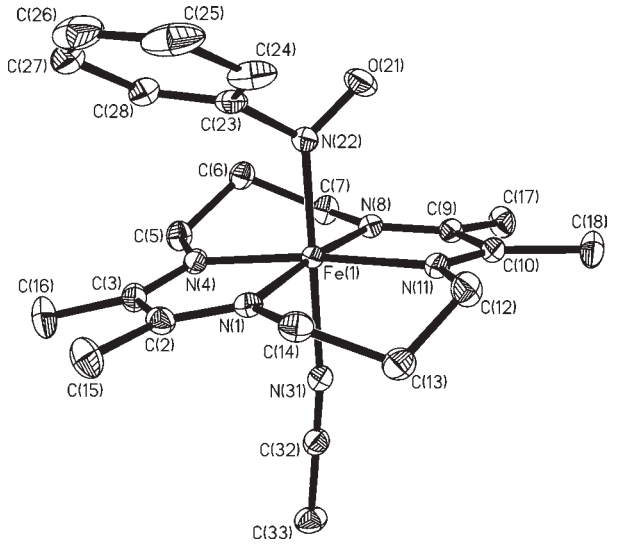

Figure 5. Crystal structure of the cationic portion of **6**; thermal ellipsoids (50%) plot. Selected bond distances [Å]: Fe−N22 1.819(1), Fe−N4 1.944(1), Fe−N8 1.946(1), Fe−N1 1.9483(1), Fe−N11 1.949(1), Fe−N31 2.001(2), N1−C2 1.290(2), N4−C3 1.289(2), N8−C9 1.285(2), N11−C10 1.289(2), N22−O21 1.240(2), N22−C23 1.465(2).

Four structural features of **6** are remarkable: (a) The Fe−N bond of the phenylnitroso group is very short at 1.819(1) Å, indicating considerable double bond character whereas both the avg. Fe−N bonds of the macrocycle $(TIM)^0$ at 1.947(1) Å and the Fe-$NCCH_3$ bond at 2.001(2) Å are normal for single bonds. (b) The N−O bond at 1.240(2) Å is longer than in **3** but shorter than in **4**. Similar Fe−N and N−O bond lengths as in **6** have been reported for related neutral $[Fe^{II}(porphyrinato)(PhNO)(L)]^0$ complexes (L = pyridine, PhNO).[75,76] (c) The main ν(NO) stretching frequency of **6** is now observed at 1363 cm^{-1} (calcd. at 1372 cm^{-1}), intermediate between Balch's complex **3** (1496 cm^{-1}, no π-back-bonding) and **4** (1316 cm^{-1}, ligand radical monoanion). (d) The 72° dihedral angle between the phenyl ring and the C−N−O plane indicates that the phenyl ring is nearly perpendicular to the CNO moiety and thus not involved in electron delocalization. Taken together, these features are consistent with metal-to-ligand π-backdonation and suggest that the electronic structure of PhNO ligands bound to transition metals is more nuanced than a simple one electron transfer scheme would suggest. Thus, to investigate these properties in more detail, we have undertaken a computational study of compounds **2**−**6** as well as a range of related RNO-bound transition metal complexes. The results of this computational study, in conjunction with the experimental data presented above, reveal a comprehensive picture of the various modes and oxidation states available to RNO ligands in coordination chemistry.

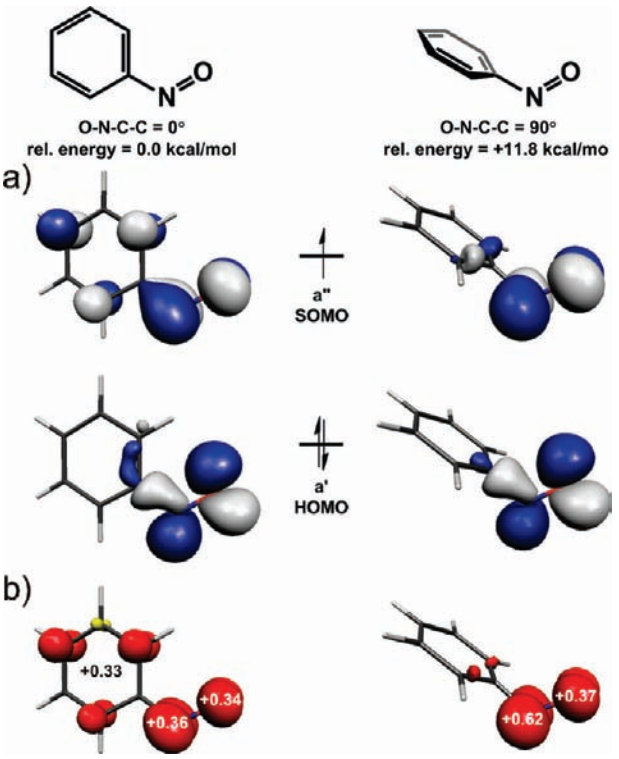

Figure 6. (a) HOMO and SOMO of uncoordinated $(PhNO)^{\bullet 1-}$ with O−N−C−C dihedral angles of 0° (left) and 90° (right). Geometry optimized bond distances in Å for the structure with a dihedral angle of 0° (90°): N−O 1.322 (1.347), C−N 1.392 (1.430). (b) Mulliken spin density distribution analyses for $(PhNO)^{\bullet 1-}$ in its geometry optimized planar configuration (left) and constrained O−N−C−C dihedral angle = 90° (right); positive spin density is shown in red, negative spin density is show in yellow.

4. COMPUTATIONAL RESULTS AND DISCUSSION

4.1. Uncoordinated $(PhNO)^{\bullet 1-}$. Figure 6 displays the highest occupied molecular orbital (HOMO) (a′) and the singly occupied molecular orbital (SOMO) (a″) of uncoordinated $(PhNO)^{\bullet 1-}$, calculated at the BP86 level of DFT along with the continuous solvation model COSMO (dielectric constant and refractive index of water). The SOMO of $(PhNO)^{\bullet 1-}$ becomes the lowest unoccupied molecular orbital (LUMO) in $(PhNO)^0$ and the HOMO in $(PhNO)^{2-}$. The electronic structure of the radical anion, where the benzene ring and the CNO plane are coplanar, is found to be 11.8 kcal/mol lower in energy than the corresponding structure where the O−N−C−C dihedral angle is constrained to 90° (the benzene ring and C−N−O plane are perpendicular relative to one another). The SOMO is π-*antibonding* with respect to the N−O bond and π-*bonding* with respect to the C−N bond. Thus, one-electron oxidation to $(PhNO)^0$ is expected to result in a shorter N−O bond and a

dx.doi.org/10.1021/ic2005979 |*Inorg. Chem.* 2011, 50, 5763–5776

Table 4. Experimental and Calculated Structural Parameters

	N−O, Å		N−C_{Ar}, Å		δ, deg		av. Pd−N_{NO}, Å		Pd−C, Å	
complexes	exp.	calc.	exp.	calc.	exp.	calc.	exp.	calc.	exp.	calc.
3	1.209(3)	1.221	1.411(3)	1.434	11.8	3.6	1.994(2)	2.023		
4	1.291(2)	1.278	1.382(2)	1.396	6.3	1.5	2.011(2)	2.083	2.004(2)	1.974
5	1.364(4)	1.340	1.432(5)	1.437			2.079(3)	2.172[a]	2.019(4)	2.003
	1.358(4)		1.441(4)				2.063(3)		1.975(4)	1.967

[a] Pd−O: experimental 2.021(3) Å (avg.), calculated 2.068 Å.

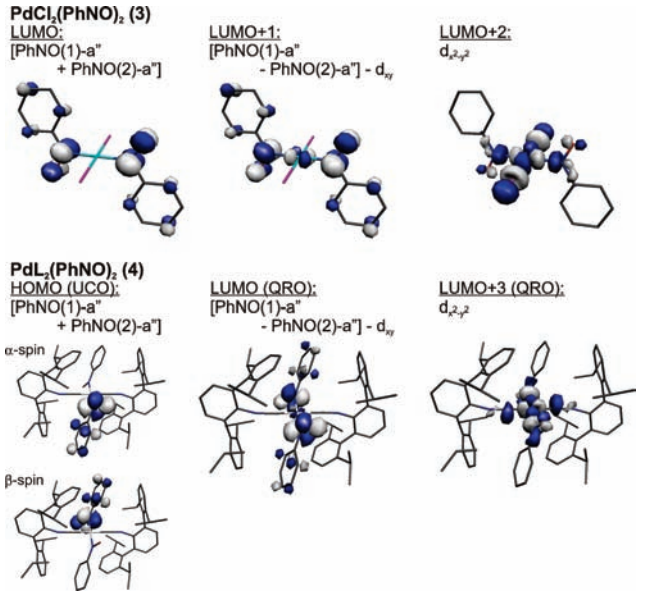

Figure 7. Comparison of the frontier molecular orbitals of **3** (top) and **4** (bottom).

slightly longer C−N bond, while one-electron reduction to $(PhNO)^{2-}$ should result in a longer N−O bond length and a shorter C−N bond. In accord with the N−O bond weakening that results from one-electron occupation of the LUMO of $(PhNO)^{0}$, the calculated N−O stretching frequencies for $(PhNO)^{\bullet 1-}$ are 1155 cm^{-1} (48% N−O character) and 1221 cm^{-1} (41% N−O character), much lower in energy than the main experimentally determined N−O stretching frequency of $(PhNO)^{0}$ at 1506 cm^{-1}[10,77] (calculated to be 1507 cm^{-1}).

4.2. Pd-(ArNO) Complexes. DFT calculations on complexes **3**, **4**, and **5** were performed using the B3LYP functional and a scalar relativistic correction using the zeroth-order regular approximation (ZORA) method. Geometry optimizations on these complexes using the X-ray structural data as starting points led to excellent agreement between theory and experiment (Table 4, Supporting Information), and the calculated ν(NO) stretching frequencies were found to match closely with those determined experimentally.

Balch's complex **3** was found to be a closed-shell, diamagnetic molecule (no broken symmetry solution), containing two neutral, η^1-*N*-coordinated $(PhNO)^{0}$ ligands. The calculated Pd−N bonds are long at 2.023 Å, consistent with Pd−N single bonds, whereas the N−O distances at 1.221 Å are short. The planar PhNO ligands in **3** are strong σ-donors and engage in only weak Pd-to-N π-back-donation. However, it is important to note that such a description for **3** reflects the weak π-basicity of the Pd^{II} center, rather than weak π-acidity of the η^1-*N*-PhNO unit, as will be discussed below. The four occupied Pd-d orbitals were clearly located in the HOMO-6 (d_{yz}), HOMO-2 (d_{z^2}), HOMO-1 (d_{xy}), and HOMO (d_{xz}), consistent with the d^8 electron count of a Pd^{II} metal center. The LUMO, resulting from the formal bonding combination of the a″ orbitals of the two PhNO units, presents no Pd-d character (Figure 7). The LUMO+1, constituting the *anti*-bonding combination of the PhNO a″-π^* orbitals, generates the local inversion symmetry needed for interaction with the Pd-d_{xy} orbital. This latter interaction is weakly antibonding, leading to a small (ca. 7 kcal/mol) gap between the LUMO and the LUMO+1.

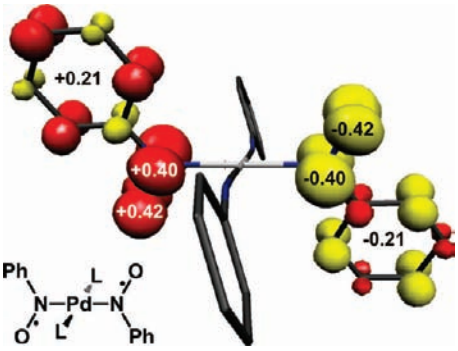

Figure 8. Calculated spin density distribution in the ground $S = 0$ state of **4** (BS(1,1), B3LYP, ZORA, α-spin in red, β-spin in yellow). The four 2,6-^{i}Pr-Ph groups have been removed for clarity.

In contrast to the closed-shell electronic structure of **3**, for complex **4** a broken symmetry BS(1,1) state ($S = 0$) was found to be 32 *kcal mol*$^{-1}$ lower in energy than the spin-restricted, closed-shell solution. Figure 5 shows the calculated Mulliken spin density plot for **4**, which clearly indicates the presence of two antiferromagnetically coupled, *N*-coordinated $(PhNO)^{\bullet 1-}$ radical monoanions (Figure 8).[78] The corresponding triplet state of **4** is only 0.4 kcal/mol higher in energy, consistent with the calculated coupling constant *J* of −114 cm^{-1}, which is in excellent agreement with the experimentally determined value of −115(2) cm^{-1}. Thus, while complex **3** is a closed-shell, diamagnetic species with an $S = 0$ ground state, **4** is a diradical with a singlet ground state and a nearby triplet excited state, comprising what can best be described as two $(PhNO)^{\bullet 1-}$ radical monoanions.

The singlet-diradical ground state can be readily explained through use of a simple molecular orbital interaction diagram and corresponding state-interaction diagram. For these purposes, we can simplify the molecular structure to a generic $L_2Pd(\eta^1$-*N*-$PhNO)_2$ formula and assume C_{2h} site-symmetry, with the *z*-axis located along the L-Pd-L vector. We can further construct the interaction diagram from a hypothetical L_2Pd fragment and a

dx.doi.org/10.1021/ic2005979 |*Inorg. Chem.* 2011, 50, 5763–5776

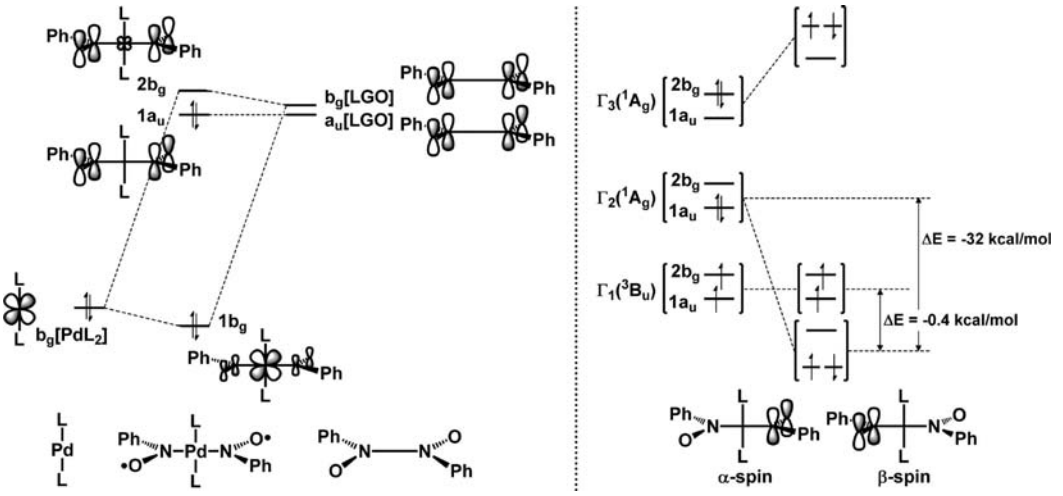

Figure 9. *Left*: Molecular orbital interaction diagram for an idealized version of **4** (see text), showing both the closed-shell electronic structure described previously for this complex as well as the origin of the small HOMO−LUMO gap. *Right*: Electronic state mixing diagram revealing the origin of the broken symmetry ground electronic state.

$(PhNO)_2$ set of ligand group orbitals (LGOs) arranged in C_{2v} symmetry (Figure 9, left). One of the essentially degenerate LGOs resulting from interaction of the a″-π^* orbitals of PhNO has the appropriate symmetry to interact with a metal d_{xz} orbital ($b_g[PdL_2]$). However, the poor π-basicity of Pd^{II} (i.e., low relative energy of the d-orbitals on Pd^{II} compared to the LUMO of neutral PhNO) results in poor overlap between the metal-d and ligand-π^* orbitals, leading to a *small* HOMO−LUMO gap between the $1a_u$ HOMO (formerly LGO-a_u) and the $2b_g$ LUMO ($b_g[PdL_2]$-b_g[LGO]). This orbital composition is directly analogous to that of complex **3**, for which the LUMO and LUMO+1 were of identical composition to the HOMO and LUMO of **4** (Figure 7). In the case of **4**, the two additional electrons enter the ligand-based $1a_u$ orbital, resulting in the electronic structure described previously for the closed-shell form of this species.[25]

The small energy difference between the occupied bonding combination ($1a_u$) and the unoccupied antibonding combination ($2b_g$), however, will allow for significant admixture of appropriate symmetry excited states into the closed-shell configuration described above, producing the singlet-diradical ground state that is stabilized from the triplet state by 2*J*. In our current scheme, this description corresponds to mixture of $\Gamma_2(^1A_g)$ with $\Gamma_3(^1A_g)$ (Figure 9, right). By virtue of symmetry, the $\Gamma_1(^3B_u)$ state is unaltered by this mixing and would therefore represent the ground state of the molecule were the Γ_2 and Γ_3 states unable to mix. In the present case, however, the state mixing produces what can be thought of as an antiferromagnetic coupling pathway, allowing the two spins to couple. This coupling pathway is composed of two independent ligand-a″-based radicals interacting with one another through the occupied Pd-d_{xy} orbital, leading to the experimentally observed, singlet ground state at low temperatures in the solid-state. This distinction between the restricted closed-shell configuration and unrestricted broken-symmetry energy surface is important for accurately describing the ground state energy and, thus, the electronic structure of this species.

Complex **5** was also investigated computationally, with a special interest in determining the origin of the bending in the isocyanide C−N−Ar group as well as the reason for the relatively short TolNO N−O bond. Geometry optimization calculations (BP86, RKS) on the full molecule of complex **5** provided excellent agreement between the calculated- and crystallographically determined structures (Table 4). The HOMO is TolNO-centered, originating from the a′ orbital of uncoordinated PhNO. This orbital character is directly analogous to the HOMO of many closely related square-planar dioxygen complexes of late transition metals. It is nonbonding with respect to the metal d-orbitals, and its location as a HOMO thus indicates that the O_2/PhNO π^* orbitals are either close to or slightly above the energy of the metal d-orbitals.

The PhNO-a″ orbital is responsible for bonding to the metal center in **5** and has the appropriate symmetry to mix with the metal $d_{x^2-y^2}$ orbital. This interaction is reflected largely in the LUMO+2 orbital, which displays Pd $d_{x^2-y^2}$−PhNO(a″) antibonding character (Figure 10). For this species, the corresponding bonding combination could not be clearly identified because of the interaction of the $d_{x^2-y^2}$ with both the σ- and π-systems of the isocyanide ligands. This mixing may account for two observed effects. The first is the effect of the nonlinear Pd−C−N angles; the bending of the isocyanide fragments is required to achieve overlap between the isocyanide π^* systems and the $d_{x^2-y^2}$ orbital on Pd. The second is the effect of the short N−O distance on the TolNO ligand. The weak σ-donor properties of isocyanides only moderately increase the energy of the $d_{x^2-y^2}$ orbital with respect to the TolNO-a″, effectively creating greater covalency in the Pd-TolNO interaction. This covalency results in a lower-than-anticipated overall electron density in the π^* system of the TolNO ligand, thereby leading to an N−O distance more reflective of occupation of the TolNO-a″ orbital with one electron than with two. Thus, the closely related Pt complex $Pt(\eta^2$-PhNO$)(PPh_3)_2$, for which the stronger σ-donor phosphine ligands will lead to a higher energy $d_{x^2-y^2}$ metal orbital, has greater polarity in the Pt-PhNO interaction, as reflected in the longer N−O bond distance of 1.410 Å.

For the sake of comparison, we also performed geometry optimization calculations on $Pd(CNPh)_2(\eta^2$-$O_2)$ (**2′**), a truncated version of the dioxygen complex **2**.[25] The optimized geometry of this truncated structure provided satisfactory agreement with the crystallographically determined molecular coordinates of **2**, with the exception of the orientation of the Ph rings

dx.doi.org/10.1021/ic2005979 |*Inorg. Chem.* 2011, 50, 5763–5776

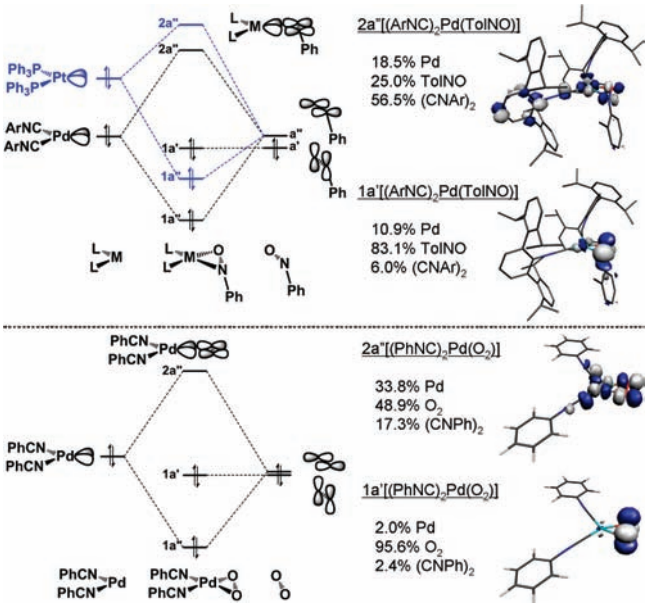

Figure 10. *Top-left*: Molecular orbital interaction diagrams comparing the mixing of $(ArNC)_2Pd$ and $(PPh_3)_2Pt$ fragments with the frontier orbitals of PhNO to produce the square-planar complexes **5** (M = Pd, L = ArNC) and $Pt(PhNO)(PPh_3)_2$. *Top-right*: Representations of the 1a′ and 2a″ orbitals for **5** along with a Löwdin population analysis. *Bottom-left*: Molecular orbital interaction diagram showing the origin of important frontier molecular orbitals of **2′**. *Bottom-right*: Representations of the 1a′ and 2a″ orbitals for **2′** along with a Löwdin population analysis.

with respect to the square plane about the metal center. This irregularity is due to the absence of the sterically demanding 2,6-(2,6-^{i}Pr$_2$−Ph)$_2$ substituents and has a negligible effect on the electronic structure at the metal center. For this species the HOMO-3 and the LUMO+2 represent the bonding and antibonding combinations, respectively, of the Pd-$d_{x^2-y^2}$ and O_2 in-plane π^* orbitals (Figure 10). The HOMO-3 is composed of 29.5% Pd and 47.4% O_2, and the LUMO+2 is 33.8% Pd and 48.9% O_2. By comparison, the LUMO+3 from a single point energy calculation on the crystallographic coordinates of **5** is composed of 25.3% Pd and 48.4% TolNO. The similarity between the calculated electronic structures for **2′** and **5**, along with the Pd K-edge XAS data, support the assignment of both species as containing Pd^{II} metal centers with two neutral isocyanide ligands, and one dianionic η^2 ligand.

4.3. $(PhNO)^0$ with π-Backbonding. With the experimental and computational data on the formal electron transfer series of $(PhNO)^{0/\bullet 1-/2-}$ in hand, we have begun to delineate the structural and spectroscopic features associated with each ligand oxidation state. An important factor to consider in this series, however, is the distinction between $(PhNO)^{\bullet 1-}$ formation and π-backdonation into $(PhNO)^0$. To examine this effect in practice, we obtained experimental data on the Fe complex **6**, for which the higher energy of the Fe-d orbitals as well as the controlled coordination environment induced by the N_4-square-planar TIM ligand led to a case in which π-backbonding would be preferred over $(PhNO)^{\bullet 1-}$ formation. Gratifyingly, the calculated geometry of the dication of **6** ($\mathbf{6}^{2+}$) agrees remarkably well with that observed experimentally, and the close agreement between the calculated and the observed Mössbauer parameters (Table 3) and ν_{NO} stretching frequencies (see above) support

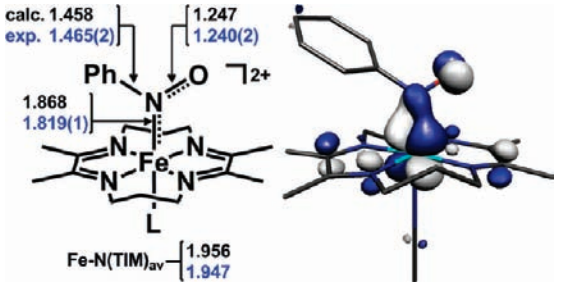

Figure 11. *Left*: Preferred resonance structure of the cationic portion of **6** with relevant calculated (black) and experimental (blue) bond lengths. *Right*: Calculated HOMO-1 of $\mathbf{6}^{2+}$; hydrogen atoms removed for clarity.

the notion that the correct electronic structure has been established. The HOMO-1 orbital, shown in Figure 11, consists of 59.3% Fe and 19.0% PhNO character and corresponds to the bonding combination of a metal-d and PhNO-a″ π-backbonding-type interaction. The experimental PhNO C−N bond length at 1.465(2) Å (calc. 1.458 Å) in **6** is the longest in the series **3**, **4**, **5**, and **6** and represents a pure single bond, while the N−O bond length of 1.240(2) Å (calc. 1.247 Å) lies intermediate between that of **3** and **4**. Together, these observations point to moderate π-acceptor ability of an *N*-coordinated neutral phenylnitroso ligand, which correlates with the relatively low contribution of the PhNO a″ fragment orbital to the HOMO-1 orbital of $\mathbf{6}^{2+}$ and is thus best represented by the resonance structure shown in Figure 11.

A critically important aspect of complex **6** is the Fe d-orbital character present in the wave function describing the NO π^* unit. This feature is distinct from both the Pd complex **4** and the other $(PhNO)^{\bullet 1-}$-containing species described below, for which full reduction to a $(PhNO)^{\bullet 1-}$ radical monoanion is represented by a singly occupied orbital exclusively of PhNO π^* character. Accordingly, these differing characteristics of κ^1-*N* coordinated PhNO ligands, determined both experimentally and computationally, firmly establish an electronic structure distinction between a $(PhNO)^{\bullet 1-}$ radical monoanion and a strong π-acid akin to carbon monoxide.

4.4. Investigation into the Electronic Structure of $(PhNO)^{\bullet 1-}$-Containing Transition-Metal Complexes. The Pd and Fe complexes described above suggest a clear relationship between the oxidation level of transition metal-bound ArNO ligands and several observables, such as (*i*) the M−N, N−O, and C−N bond distances as well as the planarity of the ArNO unit, (*ii*) the N−O stretching frequency, and (*iii*) the results of indirect measurements such as metal K-edge XAS and Mössbauer spectroscopy. Still, to expand the scope of this work and demonstrate the generality of our proposed correlation between these observable experimental features and the physical oxidation state of ArNO ligands, we have extended our computational study to a host of late transition metal RNO complexes, with a focus on investigating the electronic structure of the $(RNO)^{\bullet 1-}$ ligand. The use of ArNO as a spin-trap for transition metal-based radicals has led to a number of complexes which have been characterized via EPR spectroscopy as $(PhNO)^{\bullet 1-}$-containing species, but the instability of these complexes in solution has led to this class of complexes being largely overlooked in the literature pertaining to the coordination chemistry of RNO ligands.

4.4.1. Previously Characterized $(PhNO)^{\bullet 1-}$-Containing Complexes. As a representative example of the use of PhNO as a

dx.doi.org/10.1021/ic2005979 |*Inorg. Chem.* 2011, 50, 5763–5776

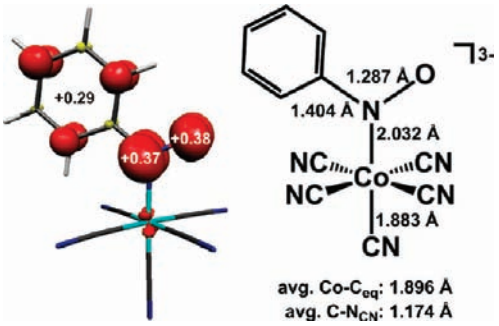

Figure 12. Calculated Mulliken spin density distribution in $[Co^{III}(CN)_5(PhNO)^{\bullet}]^{3-}$ (S = 1/2) and calculated bond distances (DFT geometry optimization, BP86/def2-TZVP, COSMO(water)).

spin-trap in transition-metal chemistry we take $[Co^{III}(CN)_5(PhNO)]^{3-}$, which is synthesized by treating a solution of $[Co^{II}(CN)_5]^{3-}$ with a solution of neutral $(PhNO)^0$ (eq 2). The product has been characterized by X-band EPR spectroscopy in solution.

$$[Co^{II}(CN)_5]^{3-} + (PhNO)^0 \rightarrow [Co^{III}(CN)_5(PhNO)^{\bullet}]^{3-} \qquad (2)$$
$$S = \frac{1}{2} \qquad S = \frac{1}{2}$$

The observed hyperfine splitting parameters of $A_{iso}\{^{59}Co\}$ = 10.3 G, $A_{iso}\{^{14}N\}$ = 13.8 G, $A_{iso}\{^{1}H_{o,p}\}$ = 3.2 G, and $A_{iso}\{^{1}H_{m}\}$ = 1.1 G as well as the isotropic g-value of 2.0051 for this compound[16] result from the presence of a low-spin Co^{III} ion (d^6, S_{Co} = 0) N-coordinated to a $(PhNO)^{\bullet 1-}$ radical monoanion. The large $A_{iso}\{^{14}N\}$, small $A_{iso}\{^{59}Co\}$, and small deviation from the free-electron g-value in this spectrum clearly rule out the alternative description of this complex as $[Co^{II}(CN)_5(PhNO)^0]^{3-}$ with an N-coordinated, neutral PhNO ligand and a low-spin Co^{II} ion (d^7, S = 1/2).[16]

The spectroscopic assignment of the $(PhNO)^{\bullet 1-}$ electronic structure on the cobalt complex was corroborated computationally by performing geometry optimization calculations using DFT (BP86) and using the continuous solvation model COSMO. Figure 12 shows the structure and the calculated spin density for the trianion. The distribution of the spin density reflects the composition of the SOMO, which is 93.8% PhNO-based. This spin density indicates that the nitrosobenzene unit is best described as a monoanionic ligand, and in accord with this description, the pseudo-t_{2g} orbitals are located at HOMO-3 through HOMO-1, with the HOMO comprising the a′ bonding combination of the in-plane PhNO π^* orbital (83.2%) with the metal d_{z^2} (8.8%). Furthermore, the calculated average equatorial Co−C bond length of 1.896 Å agrees very well with the experimental Co−C distances of 1.897 Å (avg.) in $[Co^{III}(CN)_6]^{3-}$, and the calculated N−O distance at 1.287 Å is significantly longer than in neutral PhNO at 1.20 Å. The ν_{NO} stretching frequency has been calculated at 1271 cm^{-1}; experimentally, we have observed a band for the cobalt complex at 1226 cm^{-1} by solution IR spectroscopy. These values are significantly lower than that of uncoordinated, monomeric $(PhNO)^0$ but correspond well with our computationally determined values for the N−O stretching energy of $(PhNO)^{\bullet 1-}$.

An interesting molecule for comparison is that of the EPR-characterized $Mn(CO)_5(DurNO)$ (Dur = 2,3,5,6-Me_4-C_6H), formed by photolyzing the Mn(0) dimer $Mn_2(CO)_{10}$ in the

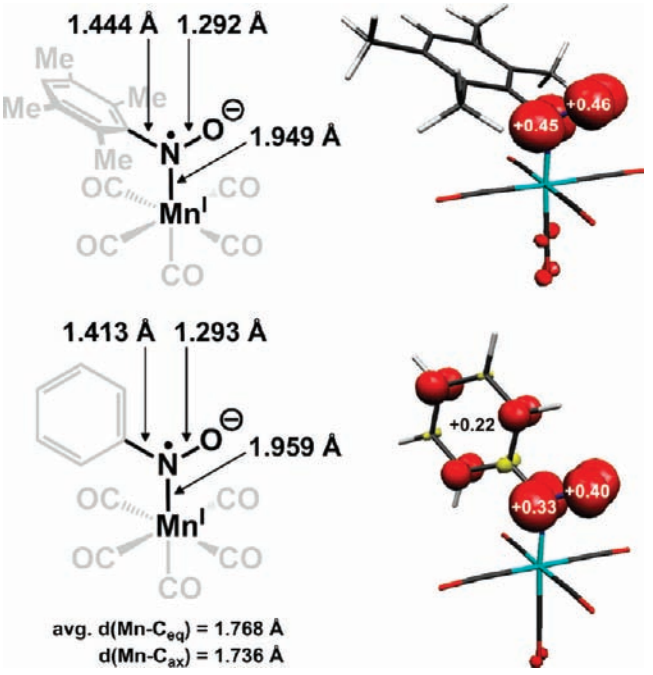

Figure 13. Depiction of important bond lengths within the geometry optimized molecular coordinates (left) and Mulliken spin density distribution analysis (right) of $Mn(CO)_5(DurNO)$ (top) and $Mn(CO)_5(PhNO)$ (bottom).

presence of DurNO.[79] The resulting experimental EPR spectrum was determined to arise from a 15.9 G coupling to nitrogen and an 8.6 G coupling to ^{55}Mn at g_{iso} = 2.006, consistent with a DurNO-centered radical with little manganese character. Furthermore, it is important to note that while the $K_3[Co(CN)_5(PhNO)]$ complex exhibited an experimental EPR coupling to the *para*-H of the PhNO ring, such a signal has not been observed for either $Mn(CO)_5(DurNO)$ or related DurNO-trapped transition metal radicals.

The geometry optimized molecular coordinates of $Mn(CO)_5(DurNO)$ reveal η^1-*N*-DurNO coordination with long N−O and Mn−N distances of 1.292 Å and 1.949 Å, respectively, consistent with formation of a DurNO radical anion, but, in this case, the steric-hindrance of the *ortho*-methyl groups prevents planarization of the nitrosoarene unit, giving an O−N−C−C dihedral angle of 87.7°. Accordingly, the molecular spin density is localized on the DurNO nitrogen and oxygen atoms (0.45 and 0.46 electrons, respectively), with <0.03 electrons on each of the aryl-ring carbons (Figure 13). The near-orthogonality of the π-system of the aryl ring with respect to the a″-symmetric, radical-containing orbital on the NO unit prevents radical delocalization. Thus, the C−N interaction at 1.444 Å is best described as a nitrogen−carbon single bond, similar to that of the analogous bond in **6**, which has a C−N distance of 1.465(2) Å. The calculated ν_{NO} for $Mn(CO)_5(DurNO)$ is 1263 cm^{-1}, similar to the values calculated for both uncoordinated $(PhNO)^{\bullet 1-}$ as well as $[Co^{III}(CN)_5(PhNO)^{\bullet}]^{3-}$.

To support the notion that nonplanarity of the DurNO unit in $Mn(CO)_5(DurNO)$ is sterically driven, we performed a geometry optimization calculation on the parent complex $Mn(CO)_5(PhNO)$, starting with the coordinates obtained from optimization of the DurNO complex. This truncated species converges on a geometry similar to that of $[Co(CN)_5(PhNO)]^{3-}$,

dx.doi.org/10.1021/ic2005979 |*Inorg. Chem.* 2011, 50, 5763–5776

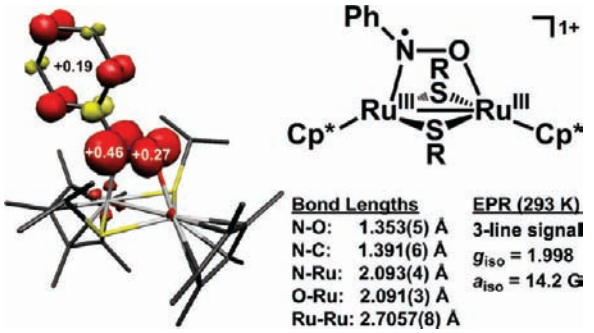

Figure 14. Calculated Mulliken spin density distribution in $[\{Cp^*Ru(\mu\text{-}S^iPr)\}_2(\mu\text{-}1\kappa^1N{:}2\kappa^1O\text{-}(PhNO)^{\bullet}]^+$ (S = 1/2; single point DFT calculation on the crystallographically determined coordinates, B3LYP/def2-TZVP, COSMO(acetone)) with experimental bond distances and EPR data from ref 23.

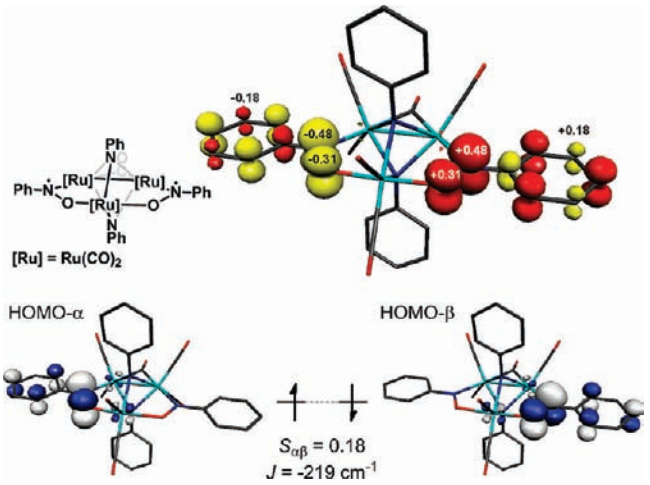

Figure 15. Calculated Mulliken spin density plot (top) and UCO orbitals (bottom) for the B3LYP geometry optimized coordinates of $Ru_3(\mu^3\text{-}NPh)_2(CO)_7(\mu^2\text{-}1\kappa^1N{:}2\kappa^1O\text{-}PhNO)_2$.

for which the PhNO ligand adopts a planar conformation (Figure 13). Similarly, $Mn(CO)_5(PhNO)$ has no spin-density on the metal center, but the planarity of the PhNO ligand allows for delocalization of the spin into the aryl ring, resulting in a strengthened N−C interaction as evidenced by the shortened d(N−C) = 1.413 Å. The calculated ν_{NO} for this species is 1246 cm^{-1}. Geometry optimization of $Mn(CO)_5(PhNO)$ with a constrained O−N−C−C dihedral angle of 87.7° results in a complex with nearly identical metric and spin-density parameters as $Mn(CO)_5(DurNO)$ but with an energy that lies +6.2 kcal/mol from the unconstrained, geometry-optimized structure.

Next, we considered what, to the best of our knowledge, are the only previously structurally characterized and appropriately described examples of $(PhNO)^{\bullet 1-}$ coordination: $[\{Cp^*M(\mu\text{-}S^iPr)\}_2(\mu\text{-}1\kappa^1N{:}2\kappa^1O\text{-}PhNO)][X]$ (M = Ru, Rh, Ir; X = OTf, BPh_4). For the Ru and Rh complexes, Hidai and co-workers reported three-line isotropic EPR spectra with g_{iso}(A_{iso})-values of 1.998(14.2 G) for Ru and 2.010(13.6 G) for Rh, fully consistent with PhNO-based radical character.[23] To corroborate the proposed electronic structure of one of these bimetallic complexes, we have performed geometry optimization calculations on the cationic portion of the Ru complex. These calculations provide excellent agreement with the crystallographically determined coordinates, and, as suggested by the experimental data, the spin-density on this complex is localized almost entirely on the bridging PhNO ligand (Figure 14). In this case, coordination of the oxygen to a second metal center is responsible for lengthening the N−O bond from the about 1.29 Å indicative of η^1-$(PhNO)^{\bullet 1-}$ (this work) to a relatively long distance of 1.353(5) Å. This increased bond length is reflected in the calculated ν_{NO}, which is predicted to lie at 1034 cm^{-1}. Interestingly, the stretching frequency for this $(PhNO)^{\bullet 1-}$ is quite low and close to the experimental and calculated values for the $(PhNO)^{2-}$-containing Pd complex **5**. This occurrence can be explained by considering that in **5** the doubly occupied a′ orbital is entirely TolNO-based, while the a″ orbital mixes with the metal $d_{x^2-y^2}$. In the dinuclear Ru complex the opposite is true: the a′ orbital forms bonding interactions with the two metal centers, while the singly occupied a″ orbital is nonbonding with the metal. The differences then are in both the occupation number of the entirely ligand-based orbital and the extent that interaction of the a′ orbital with a second metal center for the dinuclear Ru complex leads to N−O bond weakening. These effects appear complementary, leading to similar N−O bond distances and N−O stretching frequencies, even though the oxidation state of the ligand varies. The observation of the μ-$1\kappa^1N{:}2\kappa^1O$-$(PhNO)^{\bullet 1-}$ binding mode therefore speaks to the versatility of the radical anionic form of this ligand in coordination chemistry.

4.4.2. Predicted Diradical Character for RNO-Containing, S = 0 Complexes. The preceding computational results from experimentally verified $(PhNO)^{\bullet 1-}$-bound coordination complexes suggest that occupation of the PhNO-a″ orbital with one electron results in a regular lengthening of the N−O distance to about 1.30 Å, with the exact distance depending somewhat on the ligand's coordination number. In S = 1/2 systems, this ligand-based spin density may be readily observed via EPR spectroscopy, but, as we have seen for the Pd complex **4**, intramolecular antiferromagnetic coupling of two radicals can prevent the ready interpretation of the ground state electronic structure. The review of transition metal-bound organonitroso complexes written by Richter-Addo and co-workers lists a number of crystallographically characterized η^1-*N*-RNO complexes of the mid- to late-transition metals. From this list, we have taken for computational analysis two examples of complexes for which the metric parameters of the RNO ligand suggest that a formal $(RNO)^{\bullet 1-}$ formulation may have been overlooked because of the S = 0 ground state of the molecules.

First, we consider the trinuclear Ru complex $Ru_3(\mu^3\text{-}NPh)_2(CO)_7(\mu^2\text{-}1\kappa^1N{:}2\kappa^1O\text{-}PhNO)_2$,[80] for which the N−O distances of the nitrosobenzene ligands (1.334(9) Å) are well within error of the analogous N−O distance for the dinuclear Ru complex described above. The PhNO units in this species are planar, and the C−N bond lengths display the same shortening as seen for both the $[Co(CN)_5(PhNO)]^{3-}$ complex and the dinuclear Ru complex, consistent with the presence of significant electron density in the a″ orbital of PhNO. Furthermore, if one were to assume a $(PhNO)^0$ oxidation state for the two nitrosobenzene ligands, then the cluster would be described as consisting of a $Ru^{II}Ru^{II}Ru^0$ core, but the near-perfect octahedral coordination environment about each metal center suggests that either a $Ru^{II}Ru^{II}Ru^{II}$ or a $Ru^{III}Ru^{III}Ru^{II}$ core electronic structure may be more appropriate, as would be the case should the PhNO ligands adopt either $(PhNO)^{\bullet 1-}$ or $(PhNO)^{2-}$ oxidation states, respectively.

DFT geometry optimization calculations on the full molecule using the B3LYP functional (Figure 15) and assuming an S = 0

dx.doi.org/10.1021/ic2005979 |Inorg. Chem. 2011, 50, 5763–5776

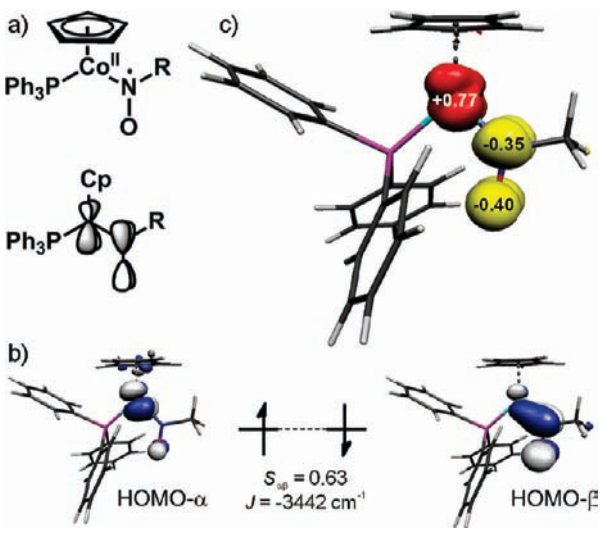

Figure 16. (*a*) Representation of the structure of $CpCo(PPh_3)(MeNO)$ along with the orbital interaction relevant to Co-MeNO π-bonding as well as diradical formation. (*b*) UCO orbitals for the HOMO of $CpCo(PPh_3)(MeNO)$. (*c*) Calculated Mulliken spin density plot for the B3LYP (BS[1,1]) geometry optimized coordinates.

ground state (determined experimentally) provided excellent agreement with the crystallographically determined structure. Furthermore, a BS(1,1) ground electronic state was found to provide a *16.4 kcal-mol*$^{-1}$ stabilization from the closed-shell solution. This BS(1,1) state can be described as comprising two $(PhNO)^{\bullet 1-}$ ligands, antiferromagnetically coupled to one another with a coupling constant J of -219 cm^{-1}. The anionic character of the nitrosobenzene ligands thus points to a $Ru^{II}Ru^{II}Ru^{II}$ core electron configuration, assuming redox innocence of the bridging imido ligands.[81] Our attempts at locating the corresponding BS(2,2), BS(3,3), and BS(4,4) states were unsuccessful, thus supporting our formulation of the trinuclear complex as $[Ru^{II}{}_3\{(\mu^3\text{-NPh})^{2-}\}_2(CO)_7\{(\mu^2\text{-}1\kappa^1N{:}2\kappa^1O\text{-PhNO})^{\bullet 1-}\}_2]^0$.

Closely related to nitrosoarene complexes are those of the nitrosoalkanes (RNO, R = alkyl), and we include here one example of such a species to support the generality of our methods for identifying RNO-based ligand redox noninnocence. The crystallographic data for the Co complexes $CpCo(PPh_3)(\eta^1\text{-}N\text{-RNO})$ (Cp = C_5H_5; R = Me, Et) reveal long N−O bond distances between 1.280 and 1.285 Å,[82,83] indicative of $(RNO)^{\bullet 1-}$ character. We have examined the methyl complex computationally and found a geometry optimized N−O distance of 1.272 Å. For this species, a BS(1,1) state was found to provide a 5.2 kcal-mol^{-1} stabilization from the closed-shell solution. This lower energy broken symmetry state corresponds to a Co(II)(S = 1/2)-$(MeNO)^{\bullet 1-}$ formulation; the strong antiferromagnetic coupling, calculated to be -3442 cm^{-1}, leads to the observed diamagnetic character of this species at room temperature. The magnetic orbitals and associated spin-density plot for the BS(1,1) state are shown in Figure 16. Both of the crystallographically characterized molecules as well as the geometry optimized structure exhibit a planar O−N−C_{RNO}−Co−P−Cp(cent) moiety, consistent with π-interaction between the (pseudo)a″ orbital of the RNO fragment and the d_{xz} orbital of the pseudo-C_s $CpCo(PPh_3)$ fragment. However, while this interaction is highly *covalent* (i.e., the two fragment orbitals contribute roughly equally to the bonding and antibonding combinations), the *magnitude* of the interaction is low (the bonding and antibonding combinations do not deviate significantly in energy from that of the fragment orbitals). The low magnitude of this interaction results from the nonideal relative orientation of the two fragment orbitals (Figure 16a). The complex's small HOMO−LUMO gap and the bonding/antibonding character of these orbitals, respectively, then allow for the admixture of electronic-excited states into the lowest-energy closed-shell configuration, producing the broken symmetry ground state that is approximated here by DFT. This description is directly analogous to that presented in detail for the Pd complex **4**, but in this case the two weakly interacting fragments are metal- and ligand-based. As is seen for nearly all metal−ligand diradical species, the coupling constant J for $CpCo(PPh_3)(MeNO)$ is large and negative, resulting from the better spatial overlap of the two "spins".

5. SUMMARY AND CONCLUSIONS

Emerging from these data are clear guidelines for assigning oxidation states within various binding modes of nitrosoarene ligands bound to transition metal ions. For the η^1-*N*-(PhNO) coordination mode, N−O bond lengths of 1.20−1.23 Å and high ν_{NO} (ca. 1400−1500 cm^{-1}) suggest $(PhNO)^0$ coordination with little or no π-backbonding, while lengthened N−O distances in the range of 1.23−1.26 Å, accompanied by shortened M−N distances and decreased ν_{NO} (ca. 1300−1400 cm^{-1}), point to considerable metal-to-ligand π-backbonding. N−O distances above 1.26 Å and below 1.31 Å appear alongside M−N distances that are consistent with M−N single bonds and point to the formation of ligands which are best described as $(PhNO)^{\bullet 1-}$, for which the ν_{NO} decreases again to the 1150−1300 cm^{-1} range. When considering coordination of PhNO to one metal center, the redox series is completed by the η^2-*N*,*O*-$(PhNO)^{2-}$ species, for which long N−O distances (>1.32 Å) and low ν_{NO} (900−1150 cm^{-1}) are indicative of N−O single bonds. Quite simply, these data reflect the effects of varying degrees of *overall* electron density (paired or unpaired) in the a″ orbital of PhNO.

In addition, we have also described several features of PhNO ligands when two metal centers are involved in binding to the nitrosoarene. In particular, the μ-$1\kappa^1N{:}2\kappa^1O$-(PhNO) binding mode may adopt either $(PhNO)^{\bullet 1-}$ or $(PhNO)^{2-}$ oxidation states. Again, the structural and spectroscopic features map with total electron density in the π^*-system of the ligand, with the μ-$1\kappa^1N{:}2\kappa^1O$-$(PhNO)^{\bullet 1-}$ oxidation state presenting N−O bond distances in the range of 1.32−1.35 Å and ν_{NO} between 1000 and 1100 cm^{-1}. The μ-$1\kappa^1N{:}2\kappa^1O$-$(PhNO)^{2-}$ oxidation state is characterized by longer N−O bond distances (1.36−1.44 Å) and lower ν_{NO} (850−1000 cm^{-1}). An interesting structural consequence of these varying oxidation states appears to be the coordination geometry of the μ-$1\kappa^1N{:}2\kappa^1O$-$(PhNO)^{\bullet 1-/2-}$ ligands. The radical anion favors a planar arrangement of the entire PhNO moiety as well as the two metal centers, while the dianion binds facially, through the a″ orbital, such that the Ph−N−O plane is nearly perpendicular to the M−N−O−M plane.

While many of the compounds investigated in this study exhibited closed-shell electronic configurations, we also found a number of examples for which clear multideterminant wave function character was evident in the ground state. Most remarkably, measurements on the temperature dependence of the magnetic susceptibility of the Pd complex **4** revealed a low energy triplet state and thus confirmed its formulation as a

dx.doi.org/10.1021/ic2005979 |*Inorg. Chem.* 2011, 50, 5763–5776

diradical species. Taking this observation into account, we performed high-level DFT calculations on this complex and found that they provided excellent agreement between the calculated and the experimental geometry, ν_{NO} stretching frequency, and antiferromagnetic coupling constant J. Moreover, the calculations found that the broken-symmetry wave function for the ground state of this species provided a 32 kcal-mol^{-1} stabilization from the restricted, closed-shell-singlet energy surface.

The clear success of these computational methods lends weight to our theoretical investigations into the ground state electronic structure of other RNO-containing $S = 0$ complexes for which the metric parameters indicate radical character in the RNO ligand. The trinuclear Ru complex $Ru_3(\mu^3\text{-NPh})_2(CO)_7(\mu^2\text{-}1\kappa^1N\text{:}2\kappa^1O\text{-PhNO})_2$ is thus believed to comprise a $Ru^{II}Ru^{II}Ru^{II}$ core with two antiferromagnetically coupled $\mu^2\text{-}1\kappa^1N\text{:}2\kappa^1O\text{-}(PhNO)^{\bullet 1-}$ radical monoanions. The low $S_{\alpha\beta}$ and small J indicate that triplet state is thermally accessible. We thus predict that variable-temperature magnetic susceptibility measurements on this species would find considerable paramagnetic character near room temperature.

At the opposite end of the spectrum for the magnitude of an antiferromagnetic coupling interaction is the Co complex $CpCo(PPh_3)(MeNO)$. For this species, the coupling of the two spins via a direct metal−ligand bonding interaction leads to a large J and thus diamagnetic character at room temperature. However, the calculated stabilization of 5.2 kcal-mol^{-1} provided by the broken symmetry energy surface is significant and thereby warrants further experimental investigation into the ground state electronic structure. Importantly, as opposed to the $S = 1/2$ complexes $[Co^{III}(CN)_5(PhNO)^{\bullet}]^{3-}$, $[Mn^{I}(CO)_5(ArNO)^{\bullet}]^{0}$, and $[\{Cp^*M(\mu\text{-}S^iPr)\}_2(\mu\text{-}1\kappa^1N\text{:}2\kappa^1O\text{-PhNO})][X]$ (M = Ru, Rh, Ir; X = OTf, BPh_4), for which the ligand radical occupies a SOMO that is entirely of PhNO character, all of the broken symmetry ground state complexes described herein are singlet diradicals, meaning that the degree of N−O bond lengthening is a reflection of the *covalency* in the HOMO.

In conclusion, we have established, both experimentally and computationally, the noninnocent redox behavior of coordinated *C*-nitrosoarene compounds. We believe such rich redox activity, which finds direct analogy with that of coordinated O_2 and NO, has been largely overlooked for this important class of ligands. Using a three-membered electron transfer series as a starting point, we have delineated the geometric, spectroscopic, and electronic structure criteria governing coordinated-PhNO as a (i) neutral π-acid and/or σ-donor, (ii) monoanionic radical, and (iii) doubly deprotonated hydroxyl amine. Additional studies exploring the effect of these differing redox states on the reactivity and spectroscopic properties of related complexes, especially those containing the monoanionic $(PhNO)^{\bullet 1-}$ radical, are underway.

■ ASSOCIATED CONTENT

Supporting Information. Complete computational details for all complexes and crystallographic information files (.cif) for complexes **5** and **6**. This material is available free of charge via the Internet at http://pubs.acs.org.

■ AUTHOR INFORMATION

Corresponding Author

*E-mail: jsfig@ucsd.edu (J.S.F.), wieghardt@mpi-muelheim.mpg.de (K.W.).

■ ACKNOWLEDGMENT

We thank Dr. Taras Petrenko for assistance with DFT calculations, Dr. Carsten Milsmann for preliminary computational work on compounds **4** and **5**, Dr. Stephen Sproules for XAS data collection, Prof. Serena DeBeer for assistance with XAS data analysis, and Prof. Arnold L. Rheingold for assistance with crystallography of complex **5**. J.S.F. and L.A.L. are grateful to the U.S. National Science Foundation for support (CHE-0954710 and an NSF-GRF), and N.C.T. thanks the Max Plank Society for financial support.

■ REFERENCES

(1) Stiefel, E. I. *Dithiolene Chemistry: Synthesis, Properties, and Applications*; John Wiley & Sons, Inc.: New York, 2004; Vol. 52.
(2) Lu, C. C.; Bill, E.; Weyhermuller, T.; Bothe, E.; Wieghardt, K. *J. Am. Chem. Soc.* **2008**, *130*, 3181.
(3) Bart, S. C.; Chlopek, K.; Bill, E.; Bouwkamp, M. W.; Lobkovsky, E.; Neese, F.; Wieghardt, K.; Chirik, P. J. *J. Am. Chem. Soc.* **2006**, *128*, 13901.
(4) Butin, K. P.; Beloglazkina, E. K.; Zyk, N. V. *Russ. Chem. Rev.* **2005**, *74*, 531.
(5) Mansuy, D.; Battioni, P.; Chottard, J. C.; Riche, C.; Chiaroni, A. *J. Am. Chem. Soc.* **1983**, *105*, 455.
(6) Eady, R. R.; Hasnain, S. S. . In *Comprehensive Coordination Chemistry II: From Biology to Nanotechnology*; McCleverty, J. A., Meyer, T. J., Eds.; Elsevier Pergamon: Oxford, U.K., 2004; Vol. 8, p 759.
(7) Kumar, M. R.; Fukuto, J. M.; Miranda, K. M.; Farmer, P. J. *Inorg. Chem.* **2010**, *49*, 6283.
(8) Paolocci, N.; Saavedra, W. F.; Miranda, K. M.; Martignani, C.; Isoda, T.; Hare, J. M.; Espey, M. G.; Fukuto, J. M.; Feelisch, M.; Wink, D. A.; Kass, D. A. *Proc. Natl. Acad. Sci. U.S.A.* **2001**, *98*, 10463.
(9) Cameron, M.; Gowenlock, B. G.; Vasapollo, G. *Chem. Soc. Rev.* **1990**, *19*, 355.
(10) Lee, J.; Chen, L.; West, A. H.; Richter-Addo, G. B. *Chem. Rev.* **2002**, *102*, 1019.
(11) Rehorek, D. *Chem. Soc. Rev.* **1991**, *20*, 341.
(12) Chaudhuri, P.; Verani, C. N.; Bill, E.; Bothe, E.; Weyhermüller, T.; Wieghardt, K. *J. Am. Chem. Soc.* **2001**, *123*, 2213.
(13) Tolman, W. B. . In *Comprehensive Coordination Chemistry II: From Biology to Nanotechnology*; McCleverty, J. A., Meyer, T. J., Eds.; Elsevier Pergamon: Oxford, U.K., 2004; Vol. 8, p 715.
(14) Whittaker, J. W. *Chem. Rev.* **2003**, *103*, 2347.
(15) Borovik, A. S.; Zinn, P. J.; Zart, M. K. In *Activation of Small Molecules*; Tolman, W. B., Ed.; Wiley-VCH Verlag GmbH & Co. KGaA: Weinheim, Germany, 2006; p 187.
(16) Swanwick, M. G.; Waters, W. A. *J. Chem. Soc. D* **1970**, 930.
(17) Swanwick, M. G.; Waters, W. A. *J. Chem. Soc. B* **1971**, 1059.
(18) Atherton, N. M.; Waldram, D. *J. Chem. Soc., Faraday Trans. 2* **1972**, *68*, 413.
(19) Basters, J. *Recl. Trav. Chim. Pays-Bas* **1972**, *91*, 50.
(20) Symons, M. C. R.; Wilkinson, J. G. *J. Chem. Soc., Faraday Trans. 2* **1972**, *68*, 1265.
(21) Waters, W. A. *J. Chem. Soc., Chem. Commun.* **1972**, 1087.
(22) Mulvey, D.; Waters, W. A. *J. Chem. Soc., Perkin Trans. 2* **1974**, 666.
(23) Iwasa, T.; Shimada, H.; Takami, A.; Matsuzaka, H.; Ishii, Y.; Hidai, M. *Inorg. Chem.* **1999**, *38*, 2851.
(24) Baldwin, D. A.; Pfeiffer, R. M.; Reichgott, D. W.; Rose, N. J. *J. Am. Chem. Soc.* **1973**, *95*, 5152.
(25) Labios, L. A.; Millard, M. D.; Rheingold, A. L.; Figueroa, J. S. *J. Am. Chem. Soc.* **2009**, *131*, 11318.
(26) Balch, A. L.; Petridis, D. *Inorg. Chem.* **1969**, *8*, 2247.
(27) Burla, M. C.; Caliandro, R.; Camalli, M.; Carrozzini, B.; Cascarano, G. L.; De Caro, L.; Gaicovazzo, C.; Polidori, G.; Spagna, R. *J. Appl. Crystallogr.* **2005**, *38*, 381.

(28) Sheldrick, G. M. *Acta Crystallogr., Sect. A: Found. Crystallogr.* **2008**, *64*, 112.
(29) van der Sluis, P.; Spek, A. L. *Acta Crystallogr., Sect. A: Found. Crystallogr.* **1990**, *46*, 194.
(30) Sheldrick, G.M. *SADABS, Bruker−Siemens Area Detector Absorption and Other Correction*; University of Göttingen: Göttingen, Germany, 2006; Version 2006/1.
(31) *ShelXTL*, 6.14; Bruker AXS Inc.: Madison, WI, 2003.
(32) Sheldrick, G. M. *ShelXL97*; University of Göttingen: Göttingen, Germany, 1997.
(33) Neese, F. *Orca, an ab initio, DFT and Semiempirical Electronic Structure Package*, versions 2.7 and 2.8; Institut für Physikalische und Theoretische Chemie, Universität Bonn: Bonn, Germany, 2009−2010.
(34) Perdew, J. P. *Phys. Rev. B* **1986**, *33*, 8822.
(35) Becke, A. D. *J. Chem. Phys.* **1986**, *84*, 4524.
(36) Becke, A. D. *J. Chem. Phys.* **1993**, *98*, 5648.
(37) Lee, C. T.; Yang, W. T.; Parr, R. G. *Phys. Rev. B* **1988**, *37*, 785.
(38) Stephens, P. J.; Devlin, F. J.; Chabalowski, C. F.; Frisch, M. J. *J. Phys. Chem.* **1994**, *98*, 11623.
(39) Schäfer, A.; Huber, C.; Ahlrichs, R. *J. Chem. Phys.* **1994**, *100*, 5829.
(40) Schäfer, A.; Horn, H.; Ahlrichs, R. *J. Chem. Phys.* **1992**, *97*, 2571.
(41) Weigend, F.; Ahlrichs, R. *Phys. Chem. Chem. Phys.* **2005**, *7*, 3297.
(42) Polarization functions from Ahlrichs and coworkers, unpublished.
(43) Eichkorn, K.; Weigend, F.; Treutler, O.; Ahlrichs, R. *Theor. Chem. Acc.* **1997**, *97*, 119.
(44) Eichkorn, K.; Treutler, O.; Öhm, H.; Häser, M.; Ahlrichs, R. *Chem. Phys. Lett.* **1995**, *240*, 283.
(45) Eichkorn, K.; Treutler, O.; Öhm, H.; Häser, M.; Ahlrichs, R. *Chem. Phys. Lett.* **1995**, *242*, 652.
(46) van Wuellen, C. *J. Chem. Phys.* **1998**, *109*, 392–399.
(47) van Lenthe, E.; Baerends, E. J.; Snijders, J. G. *J. Chem. Phys.* **1993**, *99*, 4597.
(48) van Lenthe, E.; Baerends, E. J.; Snijders, J. G. *J. Chem. Phys.* **1994**, *101*, 9783.
(49) Pantazis, D. A.; Chen, X. Y.; Landis, C. R.; Neese, F. *J. Chem. Theory Comput.* **2008**, *4*, 908.
(50) Grimme, S. *J. Comput. Chem.* **2004**, *25*, 1463.
(51) Grimme, S. *J. Comput. Chem.* **2006**, *27*, 1787.
(52) Grimme, S.; Antony, J.; Ehrlich, S.; Krieg, H. *J. Chem. Phys.* **2010**, *132*, 154104.
(53) Klamt, A.; Jonas, V.; Burger, T.; Lohrenz, J. C. W. *J. Phys. Chem. A* **1998**, *102*, 5074.
(54) Neese, F. *Inorg. Chim. Acta* **2002**, *337*, 181.
(55) Römelt, M.; Ye, S.; Neese, F. *Inorg. Chem.* **2009**, *48*, 784.
(56) Ginsberg, A. P. *J. Am. Chem. Soc.* **1980**, *102*, 111.
(57) Noodleman, L.; Peng, C. Y.; Case, D. A.; Mouesca, J. M. *Coord. Chem. Rev.* **1995**, *144*, 199.
(58) Kirchner, B.; Wennmohs, F.; Ye, S.; Neese, F. *Curr. Opin. Chem. Biol.* **2007**, *11*, 134.
(59) Neese, F. *J. Phys. Chem. Solids* **2004**, *65*, 781.
(60) Neese, F. *J. Am. Chem. Soc.* **2006**, *128*, 10213.
(61) *Molekel, Advanced Interactive 3D-Graphics for Molecular Sciences*; available at http://www.cscs.ch/molkel/.
(62) Yamaguchi, K.; Takahara, Y.; Fueno, T. In *Applied Quantum Chemistry*; Smith, V. H., Schaefer, F., Morokuma, K., Eds.; D. Riedel: Dordrecht, The Netherlands, 1986.
(63) Soda, T.; Kitagawa, Y.; Onishi, T.; Takano, Y.; Shigeta, Y.; Nagao, H.; Yoshioka, Y.; Yamaguchi, K. *Chem. Phys. Lett.* **2000**, *319*, 223.
(64) Little, R. G.; Doedens, R. J. *Inorg. Chem.* **1973**, *12*, 537.
(65) Liebeskind, L. S.; Sharpless, K. B.; Wilson, R. D.; Ibers, J. A. *J. Am. Chem. Soc.* **1978**, *100*, 7061.
(66) Berman, R. S.; Kochi, J. K. *Inorg. Chem.* **1980**, *19*, 248.
(67) Ittel, S. D. *Inorg. Chem.* **1977**, *16*, 2589.
(68) Otsuka, S.; Aotani, Y.; Tatsuno, Y.; Yoshida, T. *Inorg. Chem.* **1976**, *15*, 656.
(69) Cenini, S.; Porta, F.; Pizzotti, M.; Lamonica, G. *J. Chem. Soc., Dalton Trans.* **1984**, 355.
(70) Jones, C. J.; McCleverty, J. A.; Rothin, A. S. *J. Chem. Soc., Dalton Trans.* **1985**, 401.
(71) Pizzotti, M.; Porta, F.; Cenini, S.; Demartin, F.; Masciocchi, N. *J. Organomet. Chem.* **1987**, *330*, 265.
(72) Of the six mononuclear η^2-ArNO complexes in the Cambridge Structural Database, the N−O distances range from 1.385 to 1.431 Å.
(73) Wieghardt, K. *Adv. Inorg. Bioinorg. Mech.* **1984**, *3*, 213.
(74) Hess, C. R.; Weyhermüller, T.; Bill, E.; Wieghardt, K. *Angew. Chem., Int. Ed.* **2009**, *48*, 3703.
(75) Wang, L.-S.; Chen, L.; Khan, M. A.; Richter-Addo, G. B. *Chem. Commun.* **1996**, 323.
(76) Godbout, N.; Sanders, L. K.; Salzmann, R.; Havlin, R. H.; Wojdelski, M.; Oldfield, E. *J. Am. Chem. Soc.* **1999**, *121*, 3829.
(77) Calligaris, M.; Yoshida, T.; Otsuka, S. *Inorg. Chim. Acta* **1974**, *11*, L15.
(78) The spin density distribution within a broken symmetry singlet is a nonphysical artifact of the broken symmetry computational method. However, such spin density plots are useful representations of the multireference character of the ground state and are therefore included here for comparison with physically meaningful spin density representations.
(79) Hudson, A.; Lappert, M. F.; Lednor, P. W.; Nicholson, B. K. *J. Chem. Soc., Chem. Commun.* **1974**, 966.
(80) Lee, K. K. H.; Wong, W. T. *J. Chem. Soc., Dalton Trans.* **1996**, 3911.
(81) Lu, C. C.; DeBeer George, S.; Weyhermüller, T.; Bill, E.; Bothe, E.; Wieghardt, K. *Angew. Chem., Int. Ed.* **2008**, *47*, 6384.
(82) Weiner, W. P.; Bergman, R. G. *J. Am. Chem. Soc.* **1983**, *105*, 3922.
(83) O'Connor, J. M.; Bunker, K. D. *Organometallics* **2003**, *22*, 5268.